

Recent Progress in Optoelectronic Synapses for Artificial Visual-Perception System

Xun Han, Zhangsheng Xu, Wenqiang Wu, Xianhu Liu, Peiguang Yan,*
and Caofeng Pan*

The human visual system undertakes most of the information perceiving tasks, and nearly 80% of the perceived information is obtained via the visual system. The basic functions of the human visual system can be emulated by neuromorphic visual-perception systems in the light region from UV to near-IR. An optoelectronic synapse served as the basic unit of the neuromorphic visual-perception system is required to combine photosensing function and synaptic element. In addition, optoelectronic synapses demonstrate the prospective advantage of large bandwidth, ultrafast signal transmission, and low electrical energy loss, which is expected in the photonic signal-triggered computing. This work reviews recent progress in the optoelectrical synapses. Device architectures and working mechanisms are discussed. The applications in the artificial visual-perception system for image memorization and pattern recognition are reviewed. The main challenges and opportunities of optoelectrical synapses are also presented.

1. Introduction

The human brain is an ultimate parallel computing system, which can compute and store data concurrently in an energy-efficient manner.^[1] Neuromorphic computing was proposed in the late 1980s to mimic the way of brain process information.^[2] Significant advances have been achieved in the implementation of neuromorphic computing through the development of

software algorithms and artificial neural networks (ANNs).^[3] However, the software stimulation typically realized on the von Neumann architecture machines where numerous data transferred between processor and memory units, which are physically separated, resulting in unwanted energy consumption and the bottleneck of the computational efficiency.^[4] Such problems are expected to be solved by actualizing the massively parallel ANNs at the device and small circuit level, leading to the emerging of the artificial synapse.^[5]

The transmission, processing, and memorization of the information in the human brain mainly rely on the sophisticated neuron network, which consists of a large number of neurons (10^{11}) and their gapped junctions called synapses (10^{15}).^[6] External information can be perceived

and processed by neurons to chemical signals, and the synapses allow presynaptic neurons to transmit these signals to postsynaptic neurons through neurotransmitters.^[7] The excitatory postsynaptic current (EPSC) is induced by excitatory neurotransmitters, whereas released prohibiting neurotransmitters could lead to inhibitory postsynaptic current (IPSC). The connection strength (synaptic weight) change between two neurons relies on the recent activity of either or both sides of the synapse, which is defined as the synaptic plasticity.^[8] According to the retention time, the synaptic plasticity can be divided into short-term plasticity (STP) and long-term plasticity (LTP). STP describes the temporary synaptic weight change occurs from tens of milliseconds to a few minutes, which relates to the information processing.^[9,7b] On the other hand, LTP, including long-term potentiation and depressing, could induce the changes from minutes and hours.^[10] Long-term potentiation is the strengthening of synaptic weight, which is regarded as the foundation of memory, and long-term depression refers the weakening of the connection, associated with clearing of the unwanted memory.^[11] Spike-timing-dependent plasticity (STDP) refers to a biological process that modulates synaptic weight by the time-related presynaptic and postsynaptic spikes, which is a basic learning rule.^[12] Great efforts have been made to design the artificial synapses for emulating as much as possible neuron features, including synaptic plasticity and neural behaviors.^[13] Two-terminal synaptic devices, based on the phase-change materials,^[14] memristor,^[15] ferroelectric,^[16] or ion-migration mechanism,^[17] as well as the three-terminal and multi-terminal devices in

Dr. X. Han, Prof. P. Yan, Prof. C. Pan
College of Physics and Optoelectronic Engineering
Shenzhen University
Shenzhen 518060, P. R. China
E-mail: yanpg@szu.edu.cn; cfpan@binn.cas.cn

Z. Xu, W. Wu, Prof. C. Pan
CAS Center for Excellence in Nanoscience
Beijing Key Laboratory of Micro-Nano Energy and Sensor
Beijing Institute of Nanoenergy and Nanosystems
Chinese Academy of Sciences
Beijing 100083, P. R. China

Dr. X. Liu
Key Laboratory of Materials Processing and Mold (Zhengzhou University)
Ministry of Education; National Engineering Research Center for Advanced
Polymer Processing Technology
Zhengzhou University
Zhengzhou, Henan 450002, P. R. China

 The ORCID identification number(s) for the author(s) of this article can be found under <https://doi.org/10.1002/ssstr.202000029>.

DOI: 10.1002/ssstr.202000029

transistor architecture, have been developed and operated at a relatively low level of energy consumption.^[18] These devices are working in the electrical mode, where the synaptic behaviors are triggered by either frequency or amplitude of voltage pulses.

Eighty percent of the perceived information from the environment is obtained through the visual-perception systems.^[19] The retina detects the incident light containing the information, such as intensity, wavelength, and duration, converts it to neural pulses, and transmits them to the brain via optical nerves and synapses (**Figure 1a**).^[20] Mimicking the function of visual perception will be a critical step toward the robot vision and artificial intelligence (AI).^[21] This requires that the synapses should combine the functions of light-sensing and synaptic elements to process light signals and extract relevant information, including color, intensity, and frequency.^[22] Optoelectronic synapse is proposed to emulate the visual perception function of the retina. It is considered as another basic unit of neuromorphic computing network that using light pulse instead of electrical stimuli. Compared with the electrical-stimulated artificial synapses, the optoelectronic synapses lead to the increase in bandwidth, a decrease in interconnection energy consumption, and ultrafast signal transmission, demonstrating the potential for constructing novel ANNs.^[23]

Here, we review the recent progress of optoelectronic synapses and their applications in the artificial visual-perception systems. We discuss three architectures of the optoelectronic synapses, including two-terminal, three-terminal and integrated structure, and three working principles of charge carrier trapping and de-trapping, photoinduced valence band (VB) change, and persistence photoconductivity phenomenon. We summarize their applications in the artificial visual-perception system for image memorization and pattern recognition. Finally, we propose the remaining challenge and future requirements regarding the development of ANNs for complex functions.

2. Structure of Optoelectronic Synapses

Recently, numerous materials and architectures have been utilized to implement artificial optoelectronic synapses to emulate visual perception function.^[24] In optoelectronic synapses, the light pulses are regarded as the action potentials applied to the postsynaptic terminal, similar to external voltage stimuli of electrical synapses. Thus, device architectures of electrical synapses including the two-terminal structure and three-terminal transistor geometry could be adopted in optoelectronic synapses using the photosensitive materials.

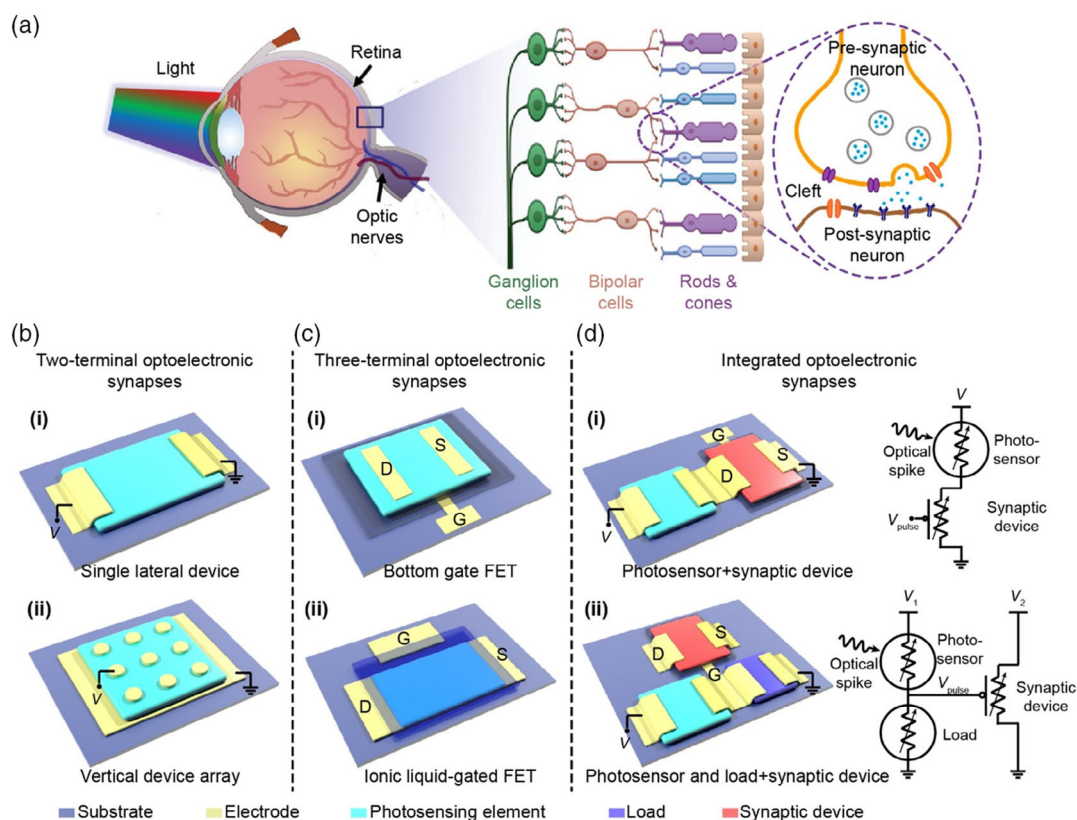


Figure 1. a) Schematic illustration of a human eye and the multilayer of the retina. Reproduced with permission.^[20b] Copyright 2020, WILEY-VCH. Structures of various optoelectronic synapses: b) two-terminal devices, i) a simple two-terminal lateral device and ii) a two-terminal vertical device array with a common bottom electrode and separated top electrodes; c) three-terminal devices evolved from i) typical bottom-gate field effect transistor and ii) ionic liquid-gated field effect transistor; and d) integration of photosensor and synaptic device, and corresponding circuit diagrams demonstrating two integration configurations: i) connecting photosensor with the conductive channel in series and ii) building photosensitive voltage divider to apply voltage pulses on presynaptic terminal.

Two-terminal optoelectronic synapses have been developed by exploiting the photosensitive memristor,^[25] persistent photoconductive effect,^[26] or photoinduced valence change mechanism (Figure 1b).^[27] It demonstrates the advantages of a simple device structure with limited unit dimensions, low energy consumption, and compatibility with the large-scale array configuration. Some basic neuromorphic characteristics, such as STP/LTP, STDP, and learning experience, have been emulated through two-terminal devices.

In three-terminal optoelectronic synapses, the gate electrode is considered as an additional terminal, and the semiconductor channel is served as the postsynaptic terminal, where channel conductivity can be modulated by either light stimuli or voltage pulse on the gate electrode. Thus, three-terminal optoelectronic synapses can operate under the combination of optical and electrical stimuli to emulate synaptic behaviors and achieve both optical potentiation and electrical depression. Either organic or inorganic materials can be worked as the conductive channel of three-terminal optoelectronic synapses in the transistor architectures, including the bottom-gate transistor, floating-gate transistor, or ionic liquid-gated transistor (Figure 1c).^[28]

Another straightforward strategy to realized optoelectronic synapses is to integrate the photosensor with an electrical-modulated synaptic device (Figure 1d). There are two structure configurations for the integration. One configuration is to connect the photosensor with the conductive channel in series and utilize the gate as the addition electrical terminal, which directly modulates postsynaptic current (PSC) under light stimuli. The other is to build a photosensitive voltage divider to generate voltage pulses with the same frequency and phase as light signals, which modulates PSC at the presynaptic terminal. The voltage divider typically consists of a photosensor and a load resistor. Both the two integrated structures could emulate synaptic behaviors successfully and endow the device with unique functions by changing corresponding components, such as to enhance the photoresponse to a specific wavelength, or realize superior flexibility or stretchability.^[29] A comparison of optoelectronic synapses with various structures and materials is summarized in Table 1.

3. Working Mechanism of the Optoelectronic Synapses

While conventional photodetectors can convert optical stimuli to electrical signals, which require fast response and recovery, the optical information cannot be stored after removing the light stimuli.^[43] In contrast, to emulate the visual-perception system, optoelectronic synapses, combining the functions of sensing and computing, demand that the photoresponse signals could be memorized at different levels to realize neuromorphic functions. Modulating the photogenerated carriers transport and recombination process to control the EPSC is the key to realize these biological functional behaviors. In this section, we summarize the working mechanism of the optoelectronic synapses and categorize them into three types: modulation of trapping and de-trapping processes of photoinduced charge carriers, photoinduced valence change mechanism, and persistent photocurrent phenomenon.

3.1. Modulation of Trapping and De-Trapping Processes of Photoinduced Charge Carriers

3.1.1. Trap States

The trap states at the interface have been widely used to control the charge carrier transport process.^[44] By controlling the trapping and de-trapping processes of the charge carriers, the conductivity of semiconductors is modulated, which is the origin of the tunable weight of synapses.^[45] Arnold et al. utilized the slow response of interface charges and trap states in the MoS₂ field effect transistor (FET) to modulate the hysteresis effect under various gate voltage.^[46] The MoS₂ FET can mimic the feature of neurotransmitter release dynamics, such as the quantal, stochastic, and excitatory or inhibitory. The surface of the Si nanocrystals (NCs) is rich in dangling bonds,^[47] which could induce energy levels beneath the conduction band (CB) to trap electrons.^[48] Tan et al. took advantage of these trap states of Si NCs to demonstrate an optoelectronic synapse with a spectral region from UV to near-IR (NIR) (Figure 2a).^[32] Under the light stimuli, the electrons in the VB are excited to the CB to generate the electron-hole pairs, which can be collected by the electrodes, leading to the increasing of EPSC. Part of the photoinduced electrons could recombine with holes immediately after light absorption, whereas part of them are trapped by the states induced by the dangling bonds. These trapped electrons could take a long time to release to the CB through thermal fluctuation and recombine with holes, contributing to the synapse plasticity (Figure 2b). Paired-pulse facilitation (PPF) is a significant STP property, which is involved in the decoding of provisional information in visual and auditory signals.^[49] PPF is a phenomenon that the postsynaptic response could be reinforced between two consecutive spikes. The Si NCs synapse demonstrated a PPF-like behavior under two identical successive laser spikes (375 nm) with an interval time of 0.2 s (Figure 2c). The EPSC evoked by the second spike (A₂) is much larger than that evoked by A₁ and gradually decays to the relatively low level in 10 s, which is attributed to the retarding recombination process of photogenerated carriers by the trap states. Benefitting from the broad light absorption spectrum of Si NCs, the synapse exhibited a wide working wavelength region from UV (375 nm) to NIR (1870 nm).^[50] Consequently, the incident power density for stimulating the same EPSC increased with the laser wavelength (Figure 2d). Furthermore, the Si NCs synapse demonstrated the transition from STP to LTP through repeat training and rehearsal (Figure 2g). Both the EPSC and retention time of EPSC significantly increased with the frequency of the laser spikes from 0.05 to 0.25 Hz. The EPSC decayed exponentially after repeating laser spikes, which is similar to the forgetting curve of the human brain. The retention time can be calculated of 106.1 s after 0.25 Hz laser spikes stimulation by fitting the decay curve with the well-known Kohlrausch function.^[51] By intercoupling two Si NCs synapses to act as the presynaptic and postsynaptic neurons, the device could mimic the STDP (Figure 2f,g). For the STDP, the presynaptic spike arrives before the postsynaptic spikes lead the potentiation of the PSC, whereas the presynaptic spike occurs after the postsynaptic spikes lead the depression of the PSC. The intercoupled device demonstrated a strong potentiation by stimulating presynaptic neuron first

Table 1. Summary of optoelectronic synapses based on various structures (2T: two-terminal; 3T: three-terminal; PSE: photosensitive element; GD: gate dielectric; CS: channel semiconductor; NW: nanowire; Dif-TES-ADT: 5,11-bis(triethylsilylethynyl) anthradithiophene; BCB: divinyltetramethyldisiloxane-bis(benzocyclobuten); and Y = “present”).

Structure	Materials	Optical spike		STP	PPF index [$A_2/A_1 \times 100\%$]	LTP	Retention time	STDP	Energy consumption	Ref.
		Wavelength [nm]	Intensity [$mW\ cm^{-2}$]							
2T	Au/LSNO/Au	365, 450, 520, 730	20–250	Y	≈ 138 , $\Delta t = 1\ s$	Y	–	–	–	[30]
	ITO/Nb: SrTiO ₃	459, 528, 630	10–30	Y	≈ 145 , $\Delta t = 0.5\ s$	Y	>3000 s	–	–	[31]
	Si NCs	375–1870	–	Y	≈ 148 , $\Delta t = 0.2\ s$	Y	–	Y	0.7 pJ	[32]
	IGZO	380–385	0.6	–	–	Y	–	Y	–	[23b]
	Pd/MoO _x /ITO	365	0.22–0.88	Y	–	Y	>300 s	–	–	[27]
3T	CS: MoS ₂ /PTCDA	532	–	Y	147, $\Delta t = 25\ ms$	Y	–	–	10 pJ	[33]
	GD: SiO ₂									
	CS: WS ₂	532	–	Y	–	Y	>1500 s	–	–	[28c]
	GD: PbZr _{0.2} Ti _{0.8} O ₃									
	CS: ZnO NW	365	0.55–17.6	Y	≈ 200 , $\Delta t = 1\ s$	Y	>800 s	–	–	[34]
	GD: SA									
	CS: pentacene	365–660	0.041–0.153	–	≈ 102 –130	Y	–	Y	1.4 nJ	[35]
	GD: PMMA/CsPbBr ₃ /SiO ₂									
	CS: Dif-TES-ADT	White light	0.03	Y	≈ 240 , $\Delta t = 0.3\ s$	Y	–	Y	–	[24b]
	GD: BCB/SiO ₂									
	CS: CuPc/p-6P	365	0.25	–	–	Y	–	–	–	[36]
	GD: SiO ₂									
	CS; IGZO	254	0.2	Y	≈ 280 , $\Delta t = 2\ s$	Y	–	–	–	[37]
	GD: HfO _x									
	CS: CsPbBr ₃ QDs/PQT-12	500	0.1	–	≈ 132 , $\Delta t = 2\ s$	Y	>2.8 h	–	–	[38]
GD: SiO ₂										
CS: pentacene	350–400	0.06–0.47	Y	≈ 120 , $\Delta t = 0.04\ s$	Y	–	–	18.06 fJ	[20b]	
GD: PMMA/NT-CN/SiO ₂										
Integrated	PSE (PTCDI-C8/VOPc)	550, 850	10.8	–	–	Y	>1800 s	–	–	[39]
	+3T synaptic device									
	PSE (In ₂ O ₃ NW) + memristor (Ni/Al ₂ O ₃ /Au)	350	0.191–0.528	–	–	–	>1 week	–	–	[40]
	PSE (WSe ₂ /h-BN) + 3T synaptic device	405, 532, 655	6	–	–	Y	–	–	66 fJ	[41]
PSE (CdSe photodetector and IGZO FET) + 3T synaptic device	465, 525, 620	7.5, 22	–	≈ 170	Y	–	–	–	[42]	

($\Delta t_{pre-post}$ is positive), whereas a weak potentiation occurred while presynaptic neuron was stimulated later ($\Delta t_{pre-post}$ is negative). Using a short spike duration (e.g., 0.2 s) and small interval time (e.g., $\Delta t_{pre-post} = -0.02\ s$), a depression behavior was demonstrated. Furthermore, the dependence of synaptic weight change, defined as $(EPSC_2 - EPSC_1)/EPSC_1$, induced by STDP on the $\Delta t_{pre-post}$ was asymmetric, which is consistent with the Hebbian rule (Figure 2h).^[52] This phenomenon was attributed to the difference of potentiation or depression when the sign of $\Delta t_{pre-post}$ changed. Ohmic contact was formed between the transparent electrode and *p*-type Si NCs, whereas the Schottky barrier with a barrier height of 0.3 eV was built at the Al/Si NC interface. Thus, when the positive bias applied (top electrode of the presynaptic neuron was connected to the anode), the Schottky barrier height in the presynaptic neuron increased, whereas the decrease in the barrier height at the postsynaptic

neuron side occurred. The photogenerated holes in presynaptic neuron needed to travel longer distance to the top electrode of postsynaptic neuron than those generated in the postsynaptic neuron. The longer drift distance resulted in higher recombination chance, which explained that the EPSC₁ became smaller, whereas EPSC₂ became larger when the presynaptic neuron was stimulated first.

3.1.2. Type-I and Type-II Heterojunctions

By elaborated designing the interfacial band alignment, heterojunctions can be adopted to trap charge carriers in the selective layers, which not only facilitates the electron–hole separation but also suppresses their recombination.^[52] The enhanced electron–hole separation efficiency could result in high photoresponsivity, whereas the suppressed recombination gives rise to the delayed

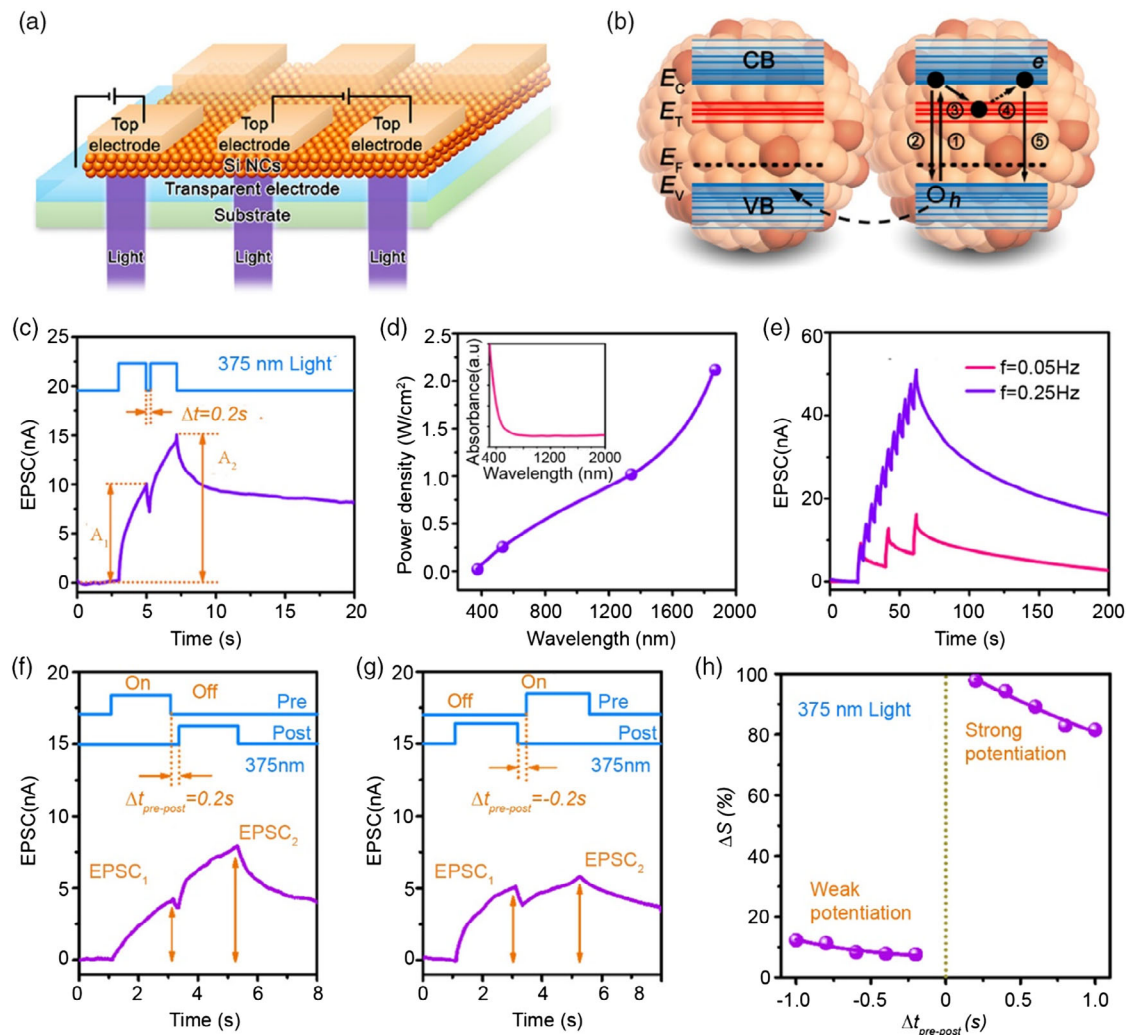


Figure 2. a) Schematic illustration of the optoelectronic synapses array based on Si NCs. b) Schematic illustration of the band structure and charge carrier transport of Si NCs. The edge of VB and CB, the trap states, and the Fermi level are expressed by E_V , E_C , E_T , and E_F , respectively. c) EPSC triggered by two successive laser pulses at 375 nm with $\Delta t = 0.2$ s. d) Required power density as a function of wavelength to achieve a ≈ 11 nA EPSC. The inset shows the distribution of light absorption about the Si-NCs film. e) EPSC under 375 nm laser spikes with the frequencies of 0.05 and 0.25 Hz for 40 s. f, g) EPSC under 375 nm laser spikes with an illumination intensity of 18 mW cm^{-2} and a $\Delta t_{\text{pre-post}}$ of 0.2 and -0.2 s, respectively. h) Dependence of synaptic weight on $\Delta t_{\text{pre-post}}$ under 375 nm laser spikes. Reproduced with permission.^[32] Copyright 2018, Elsevier Ltd.

decay of photocurrent, which is the origin of the synaptic characteristics.^[53] In recent years, utilizing a heterostructure to mimic synaptic functions has emerged as a new research area.^[54] Both type-I and type-II heterojunctions can realize the trapping of selective carriers and be utilized in the transistor architecture for introducing electrical modulation. Qian et al. utilized the copper phthalocyanine (CuPc) and para-sexiphenyl (*p*-6P) to construct a type-I heterojunction structure as the photosensitive element (PSE) to emulate an opto-synaptic behavior (Figure 3a).^[36] Due to the discontinuous crystal morphology and large energy bandgap of the *p*-6P, the carrier channel is formed in the CuPc layer. Under a 365 nm light pulse, the holes generated in the *p*-6P layer moved to the CuPc channel, whereas the electrons were trapped at the *p*-6P/dielectric interface, leading to a long retention time of the PSC (Figure 3b). Under a 655 nm light pulse, the device demonstrated a fast recovery time of the PSC

(≈ 2 s), which is because the light absorption only occurred in the CuPc layer and photogenerated carriers recombined rapidly. In addition, the CuPc and *p*-6P presented a low absorption of the 450 nm light pulse, resulting in a relatively small photoresponse (Figure 3b). The synaptic weight can be controlled by applying various gate voltages to modulate the electron trapping and de-trapping process at the *p*-6P/dielectric interface. As shown in Figure 3c, the device demonstrates three synaptic current responses under different gate voltages of -5 , 0 , and -5 V. The positive gate voltage decreased the hole conductance in the channel and trapped electrons at the interface, leading to a small PSC but long retention time (Figure 3d). In contrast, the negative gate voltage increased the conductivity of the hole channel to generate a considerable PSC but de-trapped electrons to minimize the PSC retention time. Benefiting the tunable synaptic weight, the device demonstrated long-term potentiation

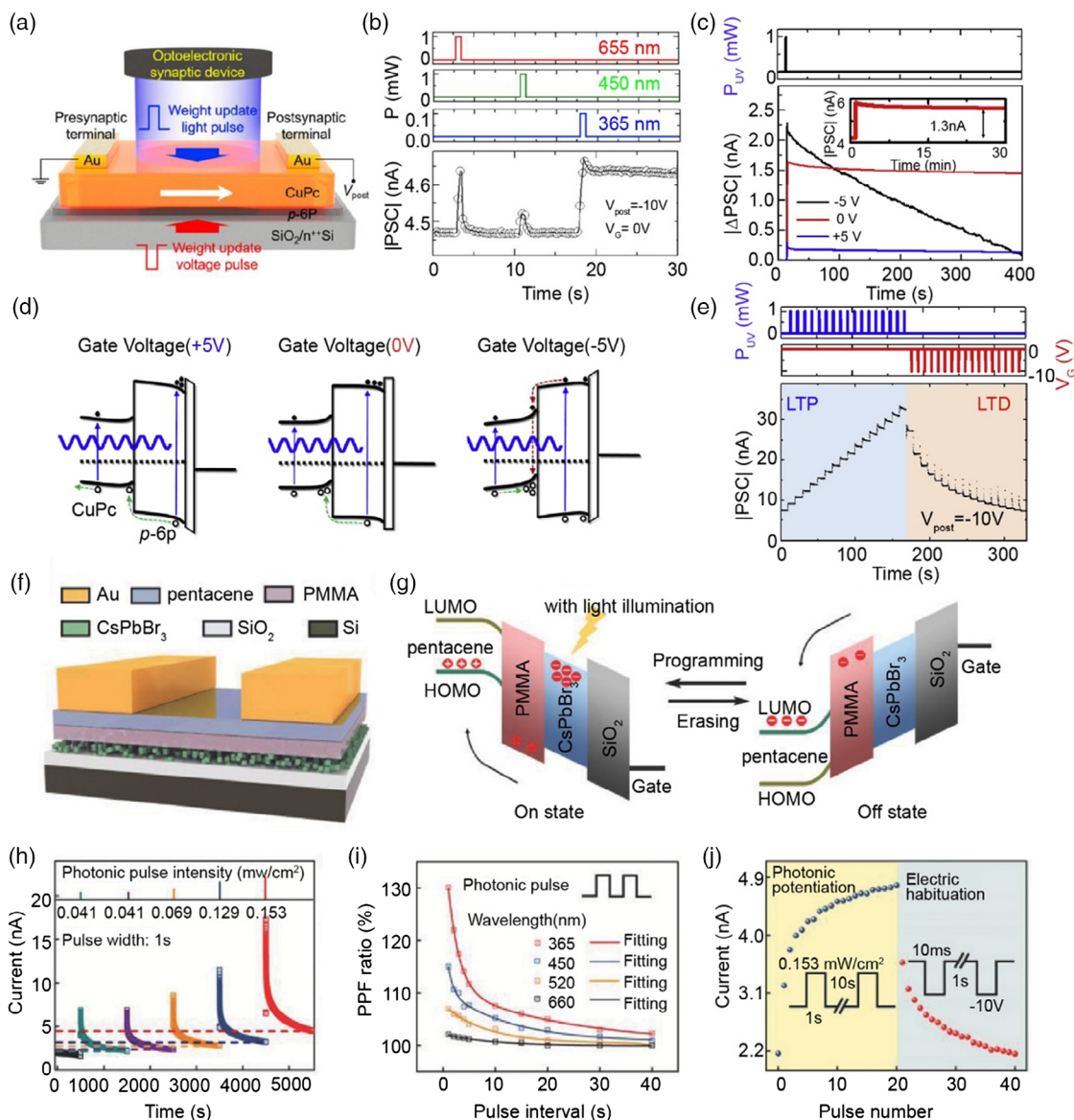


Figure 3. a) Schematic illustration of the optoelectronic synapse based on the CuPc/p-6P heterojunction. b) PSC responses under light pulses with different wavelengths (365, 450, and 655 nm). c) PSC responses under light pulses of wavelength 365 nm with different V_G values (-5 , 0 , and 5 V). d) Schematic illustration of band structure of the device under different V_G values (-5 , 0 , and 5 V). e) Long-term potentiation and depression behaviors induced by light pulses (365 nm, 1 mW, 0.5 s) and voltage pulse (-10 V, 0.1 s), respectively. Reproduced with permission.^[36] Copyright 2019, Elsevier Ltd. f) Schematic illustration of the optoelectronic synapse based on CsPbBr₃ QDs. g) Schematic illustration of the band structure of the device during optical programming and electric erasing process. h) EPSCs induced by 365 nm light illumination with different intensities. i) Dependence of the PPF effect based on four identical light pulses with a wavelength ranging from 365 to 600 nm and an illumination intensity of 0.153 mW cm^{-2} . j) Gradient channel current modulation of the synaptic device triggered by the light pulses (365 nm) and the negative voltage pulses. Reproduced with permission.^[35] Copyright 2018, WILEY-VCH.

under successive light pulses and long-term depression under negative gate voltage pulses (Figure 3e). The PSC increased with light pulses linearly and decreased for the voltage pulse exponentially. Park et al. adopt the nitric acid-treated C₃N₄ (NT-CN) layer as the floating-gate and pentacene as the channel in transistor geometry to emulate the function of UV-selective retina.^[20b] In this structure, the UV-responsive C₃N₄ layer was deposited between the SiO₂ layer and poly(methyl methacrylate) (PMMA) to domain the absorption of the UV light and trap

the photoinduced electrons. The device demonstrated a low energy consumption of 18.06 fJ per synaptic event, which is comparable to the biological synapses.^[55]

On the other hand, utilizing type-II heterojunction to trap photogenerated carriers and reduce the recombination rate to tune synaptic weight has also been paid much attention.^[38] Wang et al. demonstrated a multi-mode synaptic transistor based on the MoS₂/perylene-3,4,9,10-tetracarboxylic dianhydride (PTCDA) type-II heterojunction.^[33] In the optical modulation

mode, the photogenerated electrons injected into the MoS₂ layer rapidly, leading to a surge PSC. After light stimuli, the injected electrons returned to PTCDA gradually, resulting in the long retention time of PSC. Wang et al. reported a synaptic transistor based on the facile solution-processed inorganic perovskite quantum dots (QDs) and an organic semiconductor heterojunction structure.^[35] The device could respond to the light stimuli with a wavelength of 500 nm in a highly synapse-like fashion. To introduce the electrical control on the synaptic weight, Wang et al. introduced the CsPbBr₃ QDs floating gate in the pentacene film transistors (Figure 3f). The type-II band alignment formed between CsPbBr₃ QDs and pentacene film leads to the trapping of photogenerated charges and releasing of electrically induced charges. During the programming process, the photogenerated holes were injected into the pentacene film, leaving photogenerated electrons trapped in the active layer. These trapped electrons can be retained by the heterojunction barrier for a long time after removing light stimuli. In the erasing process, the trapped electrons were driven back to the pentacene film to recombine with the holes by the external electrical field, resulting in the decrease in PSC to the off state (Figure 3g). The device demonstrated the transformation from STP to LTP through increasing the intensity of the light stimuli (Figure 3h). The PPF ratio was obtained by applying two identical light pulses, which exhibited a dramatic decrease with the increasing of the light pulse interval and a significant increase with the wavelength decreasing from 660 to 365 nm (Figure 3i). Benefiting from the floating-gate configuration, the synaptic plasticity can be modulated by both optical and electrical stimuli (Figure 3j). The train of light pulses applied on the synapse increased the PSC to mimic the photonic potentiation, whereas the negative electrical pulse decreased the PSC that is the electric habituation.

3.2. Photoinduced Valence Change

The valence change mechanism is also associated with the resistive switching memory in the transition metal oxide-based materials.^[56] It involves migration of oxygen vacancies and anions resulting in valence change of metal cations and changes resistance by forming conductive filament between two electrodes.^[57] Zhou et al. reported a photoinduced valence change resistance memory synaptic device that exhibits light-tunable synaptic behaviors. The device adopted a two-terminal structure of Pd/MoO_x/indium tin oxide (ITO) (Figure 4a).^[27] Pd is a well-known metal catalyst for oxygen reduction reaction,^[58] which plays a key role in the reset process. The MoO_x film can absorb the UV light and generate electrons and holes inside the film. During the photoprogramming process, photogenerated holes can react with water molecules absorbed by the MoO_x film to produce protons (H⁺).^[59] Subsequently, the protons and photogenerated electrons could lead to the valence state change of Mo ions from Mo⁶⁺ to Mo⁵⁺ to form H_yMoO_x, accompanied by the color change of the MoO_x film and transition of resistance states (Figure 4b). In the reset process, protons are extracted from the MoO_x film and driven to the Pb electrode, resulting in the valence change from Mo⁵⁺ to Mo⁶⁺. The device demonstrated a clear dependence of synaptic weight on the light intensity and dosage (Figure 4c). The transition from STP to LTP was observed by applying successive

identical light pulses (Figure 4d,e). The increase in light stimuli could generate a large number of charge carriers to accelerate water dissociation reaction and further increase the possibility of valence change of Mo ions. The synaptic device arrays exhibited the ability of image memorization (Figure 4f,g). By applying larger light intensity, the letter “F” demonstrated stronger memory effect than the letter “L.” Benefiting from the light-tunable plasticity, the device demonstrated the ability of image preprocessing, including contrast enhancement and noise deduction (Figure 4h). Light pulses with different intensities were applied to the area from A to D. After 1 min, the current differences from area A to D were enlarged compared with the input image, resulting in the enhanced contrast. In addition, by utilizing pre-processed images by this synaptic device in the neural network (NN) for the image training and recognition task, both the recognition rate and accuracy could achieve obvious improvement.

3.3. Persistent Photoconductivity Phenomenon

The semiconductors that present persistent photoconductivity (PPC) phenomenon could become much more conductive under the light illumination, especially under short-wavelength light.^[60] The PPC, related to the anion vacancies in the materials, causes these semiconductors to remain conductivity for hours or days after illumination has been removed.^[61] For the photodetectors, the PPC severely degrades the recovery time.^[62] Thus, various approaches have been reported to suppress this effect, including oxygen plasma treatment, additional gate pulse to accelerate the recombination and modulation of composition ratio.^[63] However, the synaptic functions, such as STP, LTP, and STDP, could be emulated by the PPC characteristic of these semiconductors. Amorphous oxide semiconductors (AOSs), such as indium–gallium–zinc oxide (IGZO), indium–zinc oxide (IZO) indium–strontium–zinc oxide (ISZO), and indium–strontium oxide (ISO), exhibit a strong PPC behavior, which have been served as the active layer for the optoelectronic synapses.^[64] Lee et al. investigated the two-terminal photonic neuromorphic devices based on the AOSs, particularly focused on the IGZO device, to mimic the major synaptic functions (Figure 5a).^[23b] In the AOSs, the photogenerated carriers are originated from band-to-band excitation, ionization of the oxygen vacancies, and the formation of metastable peroxides. The PPC phenomenon is related to the ionized oxygen vacancies, including the single-charged V_O⁺ and doubly charged V_O²⁺.^[65] Under illumination, the oxygen vacancies are ionized to release excess electrons to increase the film conductivity. The reduction of film conductivity requires the neutralization of these ionized oxygen vacancies, which is a thermally activated process and may take a long period (Figure 5b).^[66] In general, the AOSs that possessed small bandgap, large absorption coefficient, and high concentration of oxygen vacancies should demonstrate high photocurrent. However, despite having similar bandgap and absorption coefficient in the UV region, the IGZO film with minimal oxygen vacancies exhibited the largest photocurrent and slowest decay rate among these AOSs films (Figure 5c). This is attributed to that the activation energy of IGZO required in the neutralization is largest among these AOSs, which determines the photocurrent generation, decay, and PPC behaviors. Furthermore, the PPC

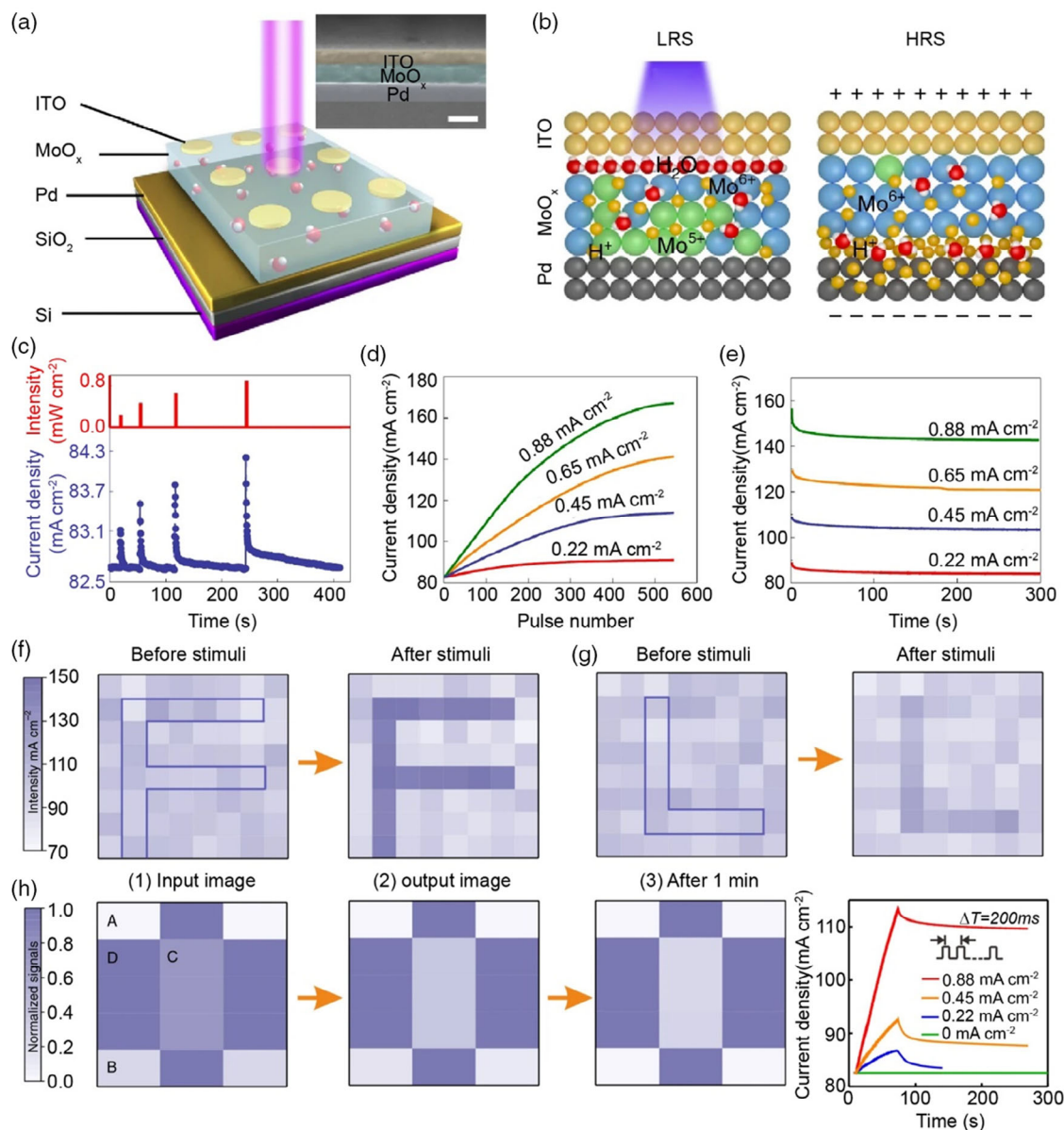


Figure 4. a) Schematic illustration of optoelectronic resistive random access memory (ORRAM) based on the MoO_x film. b) Photoinduced valence change mechanism of the MoO_x ORRAM. c) STP behavior of the ORRAM under light pulses with a pulse width of 2 s. d) Dependence of LTP on the pulse number under different illumination intensities. e) Transition from STP to LTP after 300 pulses stimulation under different illumination intensities. Schematic illustration of the image memory in f) letter “F” with an illumination intensity of 0.88 mW cm^{-2} and g) letter “L” with an illumination intensity of 0.45 mW cm^{-2} . h) Demonstration of the image contrast enhancement by the ORRAM. The right panel is the current responses during and after training. Reproduced with permission.^[27] Copyright 2019, Springer Nature.

behavior can be mediated by changing the composition ratio of the IGZO film. Wu reported the tunable photoelectric plasticity in an IGZO thin-film transistor through modulating the component content of IGZO.^[37] The IGZO film with a large In ratio exhibited large PSC (Figure 5d). An opposite trend was observed when tuned the Ga ratio, which was the Ga-enriched film demonstrated small PSC. The paired-pulse depression can also be tuned by the composite ratio. The In-enriched film demonstrated poor depression, whereas the Ga-enriched film had a strong depression effect (Figure 5e,f). Both the potentiation and depression trends are determined by the variation of carrier

concentration. Ga forms a stronger bond with oxygen than In, leading to the absence of oxygen vacancies and carriers, whereas In facilitates the formation of oxygen vacancies.^[67] Thus, the increased In proportion and decreased Ga proportion lead to a larger percentage of oxygen vacancies, which modulates the synaptic weight.

The Schottky junction between the metal and oxide semiconductors can facilitate to utilize the PPC behavior to emulate the synaptic functions. Gao et al. demonstrated a simple multi-terminal optoelectronic synapse based on the ITO/Nb-doped SrTiO_3 (ITO/Nb: SrTiO_3) heterojunction (Figure 5g).^[31] This

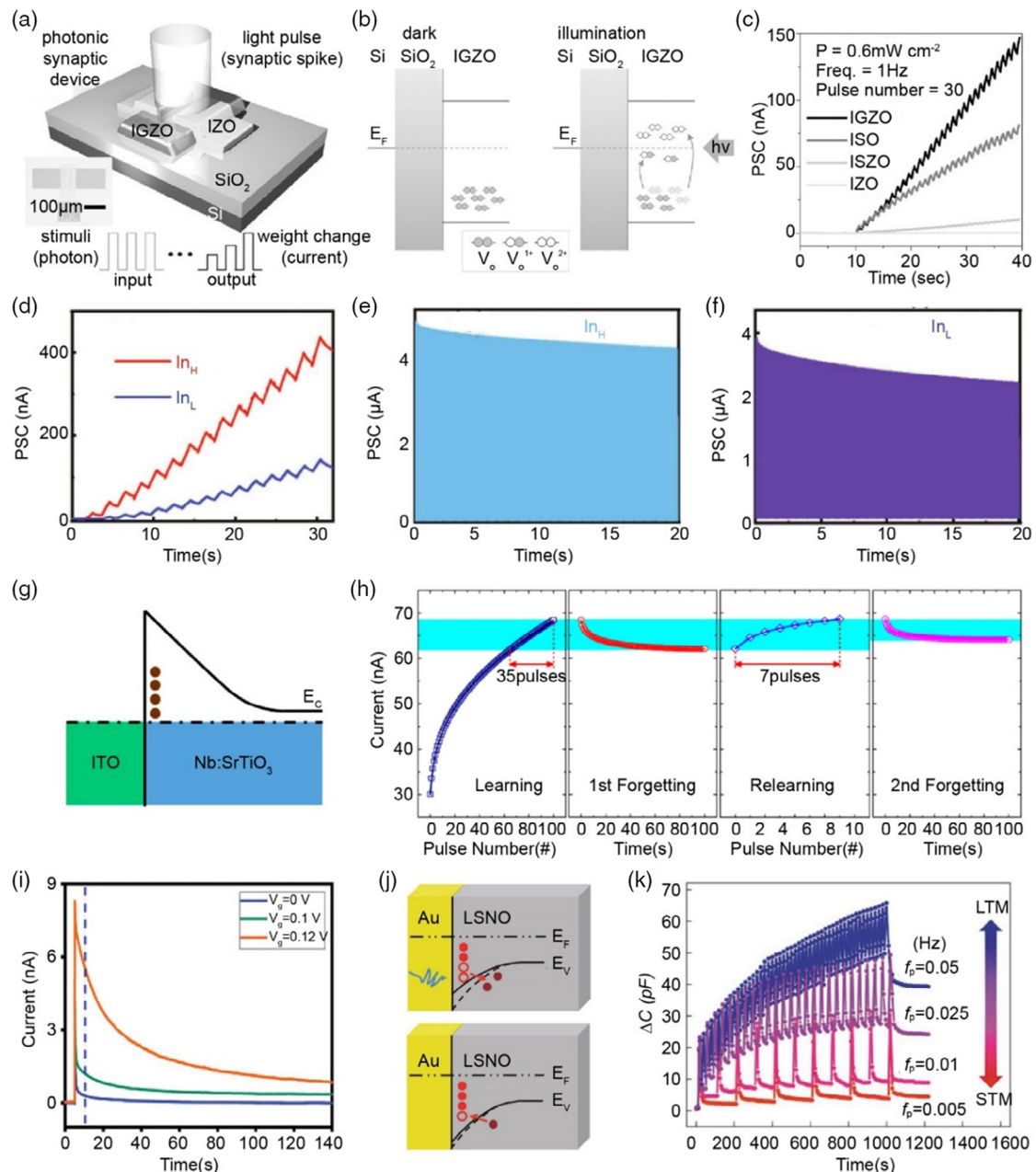


Figure 5. a) Schematic illustration of the optoelectronic synapse based on the IGZO film. b) Schematic diagram of the energy band of n-type AOS under dark conditions and light. c) The current variations under the identical UV exposure in IGZO, ISO, ISZO, and IZO devices, respectively. Reproduced with permission.^[23b] Copyright 2017, WILEY-VCH. d) The variation of the PSC under the identical pulsed UV exposure with different In ratios in IGZO film. PSC induced by electrical pulses (3 V, 100 ms) in e) In_H device and f) In_L device. Reproduced with permission.^[37] Copyright 2018, WILEY-VCH. g) Schematic illustration of Schottky barrier formed between ITO and Nb:SrTiO₃. h) “Learning-experience” behavior induced by pulsed light stimuli. Reproduced with permission.^[31] Copyright 2019, WILEY-VCH. i) EPSC of an optoelectronic synapse-based ZnO nanowire induced by pulsed light stimuli with positive gate voltages. Reproduced with permission.^[34] Copyright 2019, American Chemical Society. j) Schematic illustration of the Schottky barrier between Au and LSNO under illumination (top) and after illumination (bottom). k) Dependence of the transition from short-term memory (STM) to long-term memory (LTM) on the frequency of pulsed light stimuli. Reproduced with permission.^[30] Copyright 2019, WILEY-VCH.

optoelectrical synapse works on the principle of the PPC phenomenon of the Nb: SrTiO₃ film. Besides the STP, LTP, and PPF, this synapse demonstrated the “learning-experience” behavior of human brains (Figure 5h). Only seven light pulses were needed in the second stimulating process to recover

decayed PSC, which took 35 light pulses to realize the identical PSC in the first stimulating process. The photoplasticity of this synapse can be modulated under a sub-1 V external voltage. Sun et al. demonstrated a flexible optoelectronic synapse based on the ZnO nanowires and sodium alginate (SA) in the

ionic-gated transistor geometry.^[34] The photoinduced oxygen releasing and PPC behavior in ZnO nanowire gave rise to the synaptic plasticity. The EPSC could be triggered by both electric pulses through the gate electrode and light stimuli (Figure 5i). In the Schottky junction, the PPC phenomenon can cause the persistent capacitance of the junction. Zhao et al. proposed a photoelectric memcapacitor based on the planar Au/La_{1.875}Sr_{0.125}NiO₄ (LSNO)/Au metal/semiconductor/metal structure and utilized the capacitance change to characterize the synaptic weight (Figure 5j).^[30] It worth noting that the varied frequency of optical pulses can cause the capacitance change and modulate synaptic functions (Figure 5k).

4. Optoelectronic Synapses for Artificial Visual-Perception System

Numerous artificial optoelectronic synapses have been developed by combining the PSEs with two-terminal memristor, three-terminal transistor, and hybrid device architecture. Basic synaptic functions can be achieved under different types of light stimuli. The human visual system could transform the light information, such as wavelength, intensity, and frequency, to nerve impulses and transmit them through optical nerves to the visual cortex for interpretation. To mimic the visual-perception function of human, ANNs by integrating these optoelectronic synapses have been demonstrated. In this section, we will introduce artificial visual-perception systems with the function of image memorization and pattern recognition.

4.1. Image Memorization

A straightforward strategy to realize the image memorization function is to integrate the photosensors with memory devices. The two-terminal memristor, which relies on establishing conductive filament to switch resistance states, has demonstrated the ability to mimic the biological synapses.^[68] Chen et al. demonstrated a visual memory system by integrating a photodetector with a memristor, which can store the captured image for 1 week.^[40] The device comprises an In₂O₃ nanowire photodetector and an Al₂O₃ memristor, which are connected in series (Figure 6a). The photodetector exhibited stable photoresponse under UV illumination, and the resistance states of the memristor can be controlled by the external voltage (Figure 6b,c). Under the UV illumination, the decreased resistance of the photodetector leads to the increasing of partial voltage on the memristor to the set voltage, resulting in the transformation from “off” state to “on” state to store light information (Figure 6d). After removing the UV illumination, the “on” state could be maintained until applying a reset voltage (Figure 6e). A 10 × 10 visual memory array was fabricated to detect and store images (Figure 6f). A butterfly shaped UV light pattern was applied to the array. The pixels exposed to the UV light can switch the resistance states from “off” to “on” under a positive voltage sweep from 0 to set voltage. A clear butterfly shaped pattern can be recognized through the readout resistance states from all pixels and maintained for 1 week at room temperature. The device can be initialized by applying a negative-reset voltage and detect a butterfly shaped

or heart-shaped light pattern again, revealing the capability of write, store, and erase information for multicycles.

Neuromorphic transistors could possess several gate terminals to receive stimuli from many sources, which could realize complicated synaptic functions.^[69] Kwon et al. reported an environment-adaptable optoelectronic synapses array to emulate synaptic functions under photopic and scotopic conditions.^[42] The device consists of a photovoltaic divider based on the CdSe photosensor and a-IGZO transistor, and an ionotronic synaptic transistor (Figure 7a). Under the light stimuli, the photovoltaic divider provided voltage pulses to the gate electrode of the synaptic transistor, resulting in the modulation of synaptic weight. The photovoltaic divider could distinguish specific light intensities of different wavelengths (red, green, and blue), and amplitude of output voltage depends on the resistance ratio between CdSe photosensor and a-IGZO transistor (Figure 7b). By applying ten pulses of visible light illumination, the EPSC from the synaptic device was successfully be triggered, demonstrating LTP and STP behaviors under a light intensity of 22 and 7.5 mW cm⁻², respectively (Figure 7c). Through the a-IGZO transistor gate control, the device demonstrates the concept of photopic and scotopic adaptation. A 3 × 3 device array was utilized to demonstrate the light adaptation function (Figure 7d,e). An “H”-shaped light pattern was applied to the array with different pixels under various illumination intensities from 10.5 to 43.5 mW cm⁻². In the high illumination intensity condition, the image pattern could be recognized with the gate voltage of 0.24 V (Figure 7d). However, the EPSCs from pixels under a small illumination intensity of 10.5 and 22 mW cm⁻² faded away within 1 s with a gate voltage of 0.24 V, and a retention time of these pixels increased to 10 s while decreased the gate voltage to 0.22 V (Figure 7e). Therefore, in the bright environment, the gate voltage should be enlarged to distinguish the light intensity of the visual image (photopic adaptation), while to decrease the gate voltage for light information perceiving in weak-light condition (scotopic adaptation).

Flexible devices are regarded as a potential candidate for the rapid advancing applications, such as environment monitoring,^[70] wearable devices,^[71] healthcare monitoring,^[72] and soft robotics.^[73] An ultraflexible, light-triggered organic neuromorphic device (LOND) based on the organic electrochemical transistor and light-sensitive element was fabricated for the artificial visual-perception systems (Figure 8a).^[39] A p-type copolymer was selected as the channel material, and poly(vinylidene-fluoride-co-trifluoroethylene) [P(VDF-TrFE)] and poly[(1-vinylpyrrolidone)-co-(2-ethyl-dimethylammonioethyl methacrylateethyl sulfate)] [P(VP-EDMAEMAES)] were served as the gate dielectric. The synaptic transistor demonstrated three types of plasticity, including electrochemical STP/LTP and ferroelectric LTP. The light-sensitive element provided light related output voltage to modulate the synapse, which consisted of an organic heterojunction [dioctyl substituted perylene tetracarboxylic diimide (PTCDI-C8)/vanadyl phthalocyanine (VOPc)] to absorb light stimuli and a load resistor. They developed a water-aided peeling-off approach to facilitate the device fabrication on the ultrathin substrate and laminated the device on a hemispheric surface to mimic the function of the retina (Figure 8b). Under the green light (550 nm, 8 Hz) stimuli, the PSC became 2.9-fold higher than the initial state at a small intensity of 0.025 mW cm⁻², whereas permanent PSC change by 3 × 10³ occurred at a large intensity of 26.10 mW cm⁻²

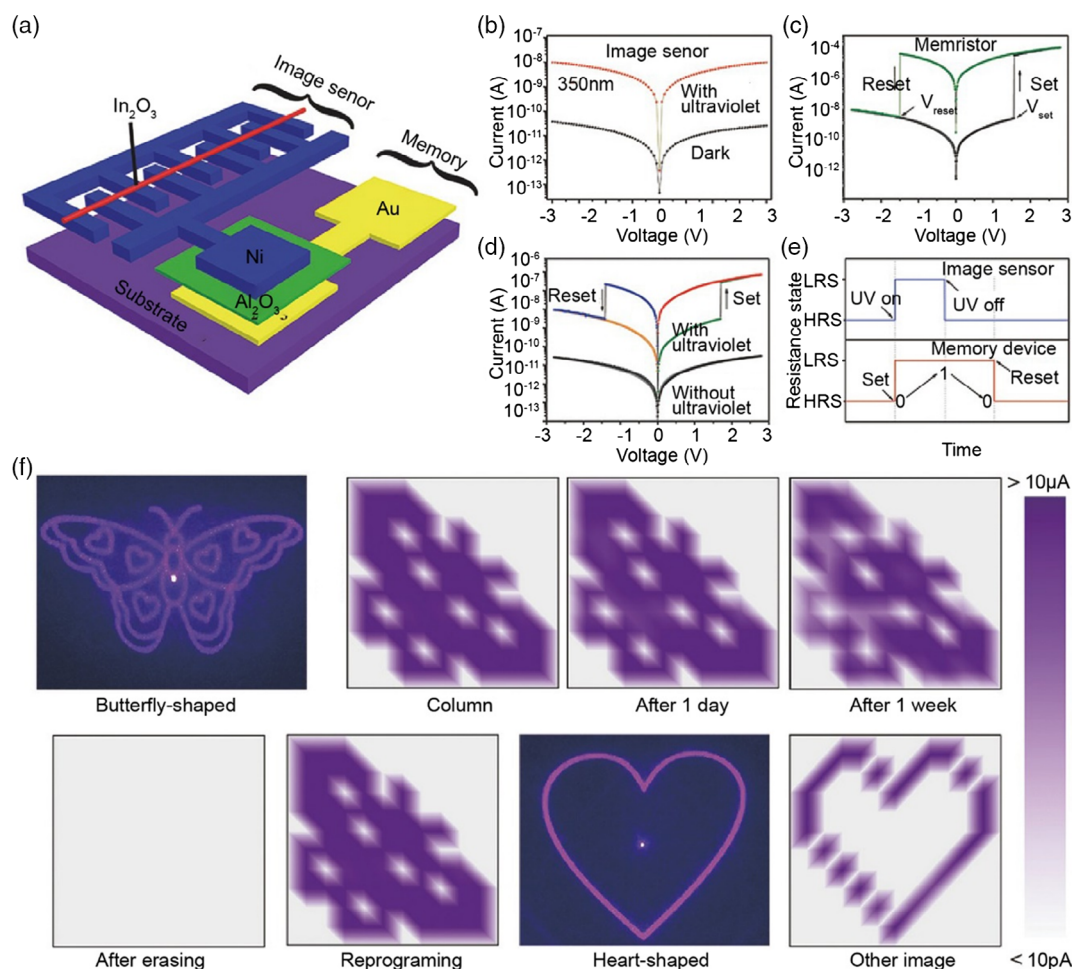


Figure 6. a) Schematic illustration of the vision memory device composed of an image sensor and a memristor. b) I - V curves of the image sensor under dark and UV light illumination. c) I - V curves of the memristor. d) I - V curves of the bio-inspired vision memory device with and without UV light illumination. e) Schematic illustration of resistance switching behavior under light stimuli and voltage sweep. f) Information storage of patterned illumination in vision memory device. Reproduced with permission.^[40] Copyright 2018, WILEY-VCH.

(Figure 8c). This is attributed to the transition from intensity-dependent electrochemical LTP to ferroelectric LTP. In the ferroelectric mode, the device achieved the capability of gray-scale green-light perception (Figure 8d). In addition, the synaptic signals can also be evoked by the 850 nm light stimuli (Figure 8e). However, due to the wavelength selectivity, the device demonstrated weaker photoresponse under 850 nm light stimuli than 550 nm. The device was stimulated by two kinds of illumination with different wavelengths but identical intensity and frequency to characterize the color-perception function. Under the NIR illumination (850 nm), the device was triggered to electrochemical LTP mode, in which the PSC fade away within 1800 s (Figure 8f). In contrast, the 550 nm light illumination evoked large PSC, which decayed 35% after 1800 s (Figure 8g). Thus, by characterizing the decay degree of PSC, the device could realize the wavelength-recognition function.

4.2. Pattern Recognition

Pattern recognition tasks have been enabled by the ANNs built by synaptic devices.^[74] The emerging optoelectronic synapses

provide new opportunities for ANNs to realize the recognition of complex patterns, including colored and color-mixed patterns. Seo et al. demonstrated an optic-neural synaptic device based on an hexagonal boron nitride (h-BN)/WSe₂ van der Waals heterostructure (Figure 9a).^[41] In the synaptic device, the conductivity of the WSe₂ channel was tuned by the electrons trapping and de-trapping process in the weight control layer on the top surface of h-BN. In the photodetector, the resistance of the h-BN/WSe₂ structure was modulated by the incident light wavelength, including 405 nm (blue), 532 nm (green), and 655 nm (red). The synaptic functions of the device were investigated under different wavelengths. The light with shorter wavelength could induce large conductance change; however, the shape of LTP/LTD curves was independent of incident light color (Figure 9b). The conventional NN without the optical-sensing function and optical-neural network (ONN) was adopted to conduct the recognition task of colored and color-mixed patterns (Figure 9c). The input layer consisted of a 28 × 28 array, which was separated into three neurons, and each pixel in the array demonstrated different responses to the light color of red, green,

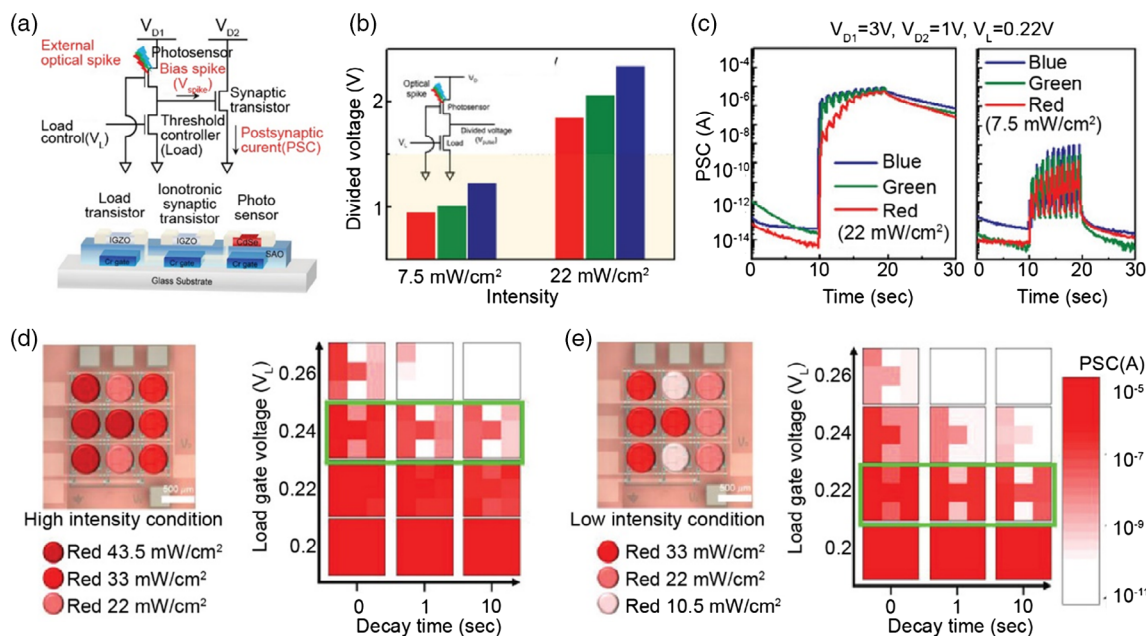


Figure 7. a) Schematic illustration of the circuit and structure of the environment-adaptable optoelectronic synapse. b) Output divided voltages under visible-light spikes with an intensity of 7.5 and 22 mW cm⁻², respectively. c) EPSC induced by visible-light spikes. The 3 × 3 optical images recorded after red light irradiation and dependence of PSC on decay time under d) a high intensity range from 22 to 43.5 mW cm⁻² and e) a low intensity range from 10.5 to 33 mW cm⁻². Reproduced with permission.^[42] Copyright 2019, WILEY-VCH.

and blue; 600 images with colored numbers “1” and “4” were utilized as the training set, and the test set consisted of 180 images of the color-mixed number “4” (Figure 9d). The target of this recognition task is to identify the numbers buried in the color-mixed images. After 50th training epoch, the ONN demonstrated a higher recognition rate than the NN, and the rate for ONN could reach and be stable at 90% (Figure 9e). The synaptic weight values could also be visualized after the 12th and 600th epoch, with blue patterns demonstrating richer weight than the green and red patterns, which indicates the capability to recognize the colored numerical patterns (Figure 9f). In addition, the ONN also exhibited, satisfying recognition ability in the color-mixed pattern recognition task (Figure 9g). The ONN achieved a higher activation score than the NN while recognized the red number “1.” Building ONNs will be a critical step to realize complex pattern recognition.

Real-time recognition and dynamic image capturing rely on the fast response and high-speed processing of the visual systems, which is critical to delay-sensitive applications, such as robotics and autonomous vehicles. In the conventional AI vision sensor, the visual information is captured through the photodetector, then, converted to digital form, and fed as input to the external ANN for sequent image processing (Figure 10a). In this process, all the optical information including a large amount of redundant data is transited to the ANN, resulting in slow response and high-power consumption.^[75] To address this issue, Mennel et al. proposed a novel visual system combining the functions of photosensing and neuromorphic computing (Figure 10b).^[77] This system could filter redundant data and transfer the reduced data to the external circuits to realize rapid response. Wang et al. demonstrated a reconfigurable NN vision sensor network to emulate the hierarchical connectivity among neurons for simultaneous sensing and image preprocessing.^[76]

The device was based on the WSe₂/h-BN/Al₂O₃ vertical heterostructure and demonstrated both positive and negative photoresponses dependent on different gate voltages (Figure 10c). Under the light illumination, the electron–hole pairs were generated in the WSe₂ channel, whereas the electrons of the point defects in the h-BN layer were excited. When the gate voltage was 0 V, the photoinduced electrons and holes in the WSe₂ channel gave rise to the positive current change, indicating the ON-photoresponse feature (upper panel, Figure 10c). By applying the negative gate voltage, the photoexcited electrons in different layers of h-BN migrated upward and recombined with the positively charged defects in the upper layers, leaving positively charged defects located at the h-BN/Al₂O₃ interface to screen the back gate electric field and suppress the conductivity of WSe₂ channel, resulting in the OFF-photoresponse feature (lower panel, Figure 10c). The biological receptive field (RF), which is critical for extracting key features of images at the early visual signal processing stage, was emulated through a vision sensor array consisted an OFF-photoresponse device surrounded by 12 ON-photoresponse devices (Figure 10d). The RF possessed a center area and surrounding areas and was characterized by the difference-of-Gaussians model (DGM). Detecting of object edges, a basic function of the biological RF, was realized through the vision sensor array. With the edges moving to the right side, the output current of the array increased, as more ON-photoresponse device was activated under light illumination. With continuous movement, a drop of the output current occurred due to that the OFF-photoresponse device was illuminated, representing the dynamic response to the edge moving (right panel, Figure 10d). In addition, the vision sensor array demonstrated the ability of simultaneous image sensing and processing (Figure 10e). Through assigning specific gate

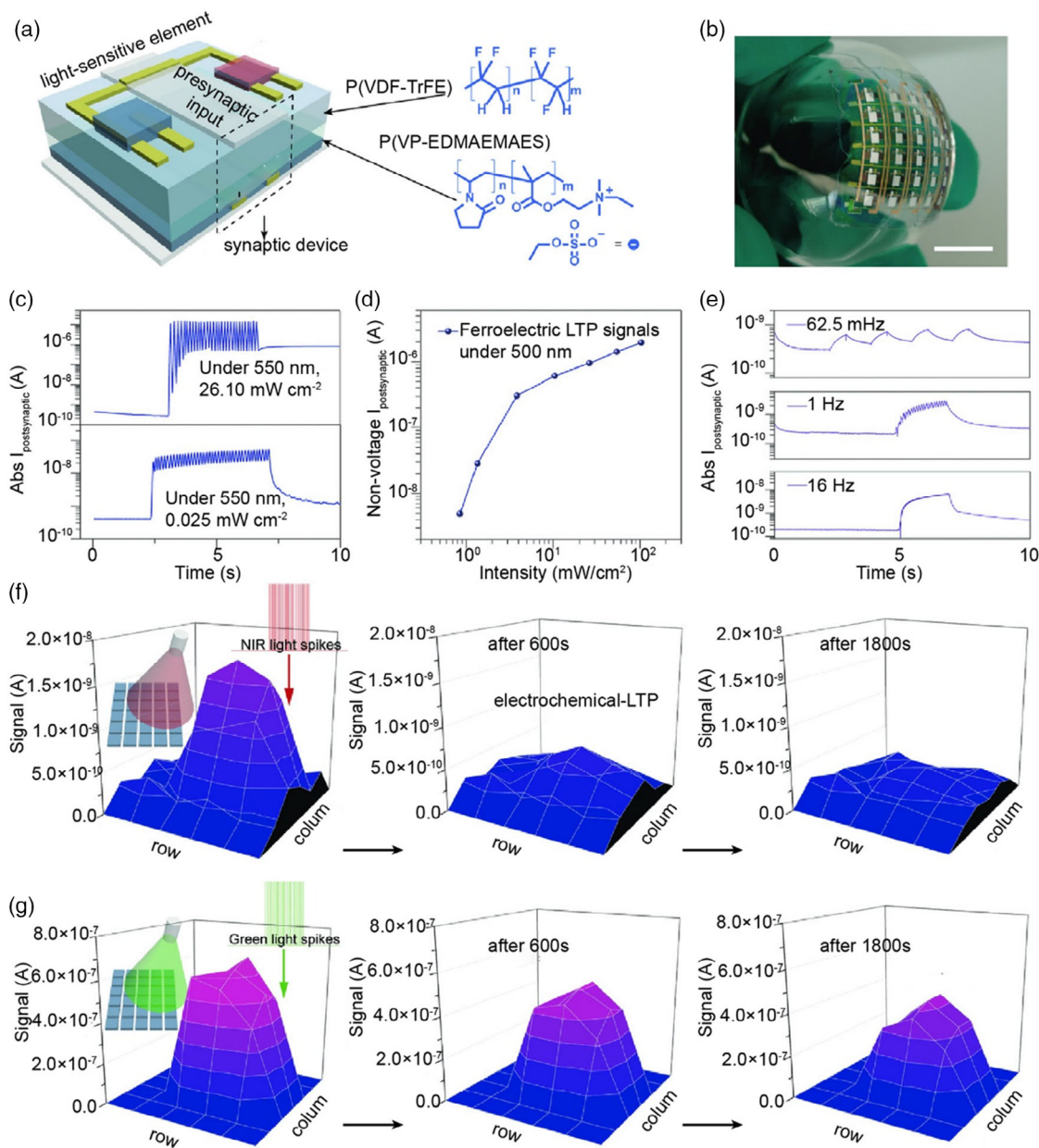


Figure 8. a) Schematic illustration of the LOND's structure and chemical structures of P(VDF-TrFE) and P(VP-EDMAEMAES). b) Optical image of an LOND array laminated on a hemisphere to mimic the retina. c) Transition from STP to LTP of the LOND array. d) Non-volatile postsynaptic signals of LOND under 550 nm illumination. e) The signals of LOND under 850 nm light illumination with different frequencies. f) Signals of the LOND array right after removing NIR light spikes and remnant signals after removing NIR light spikes for 600 and 1800 s. g) Signals of the LOND array right after green light spikes and remnant signals recorded after removing green light spikes for 600 and 1800 s. Reproduced with permission.^[39] Copyright 2018, WILEY-VCH.

voltage to each device, the difference-of-Gaussian kernel was achieved in the vision sensor array. An image of the edge enhanced letter “N” was demonstrated by reconstructing the data of the current variance with good agreement between the experimental results and simulation results (Figure 10f). The vision sensor array further exhibited promising applications in image stylization, contrast correction, noise reduction, and real-time tracking through modulating gate voltage individually of each device.

5. Conclusion and Outlook

As a basic unit of the neuromorphic computing network, great efforts have been made to design and fabricate novel optoelectronic synapses, aiming for low energy consumption, fast signal transition, and complex neural function actualization. Here, we reviewed the state-of-the-art optoelectronic synapses with device structures, working mechanism, and their applications in the artificial visual-perception systems for image memorization

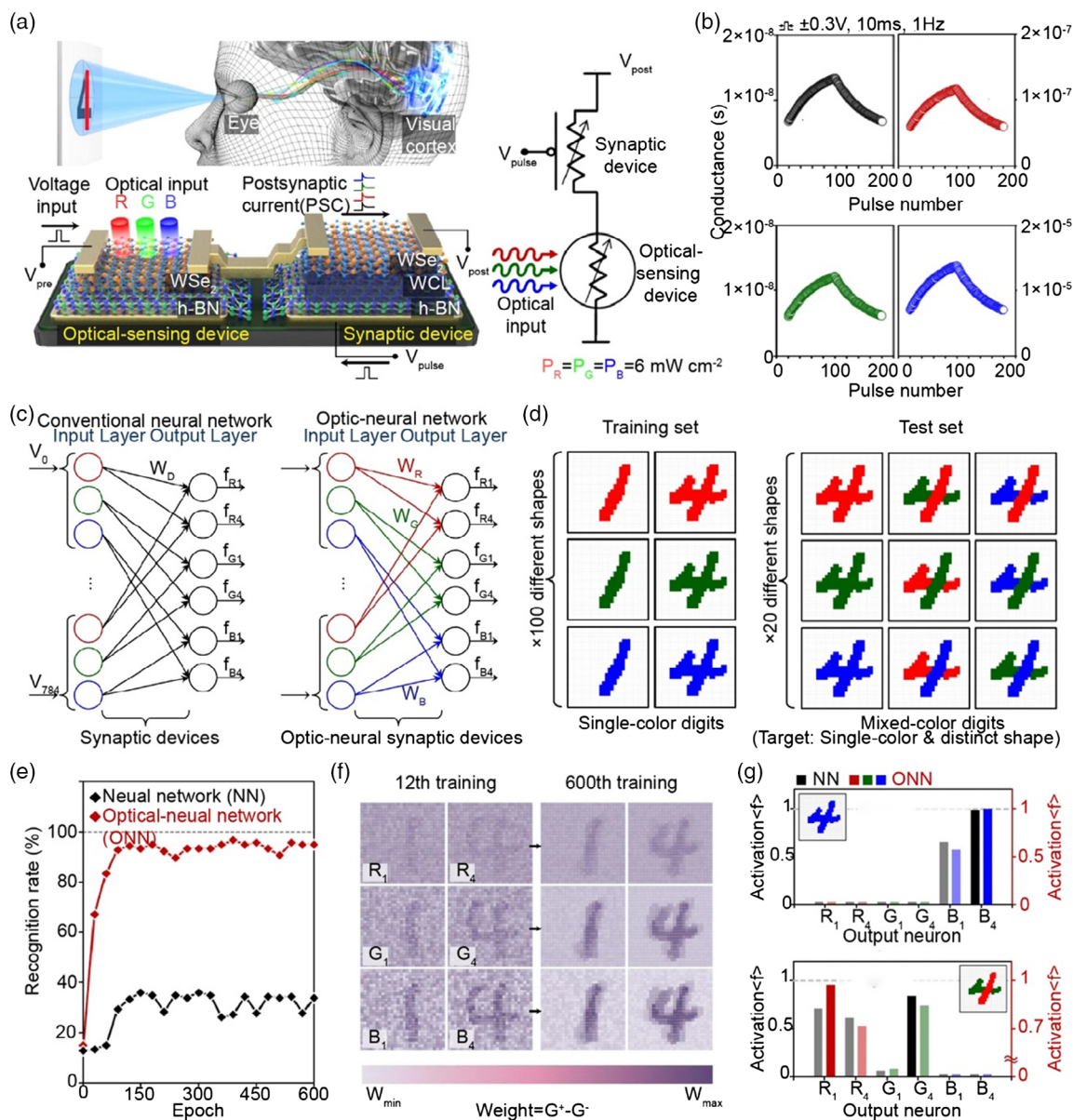


Figure 9. a) Schematic illustration of the human optic nerve system and the optoelectronic synapse integrated by the optical-sensing device and synaptic device. b) Long-term potentiation and depression behaviors under light illumination with different wavelengths. c) Schematic illustration of conventional NN and ONN for the colored and color-mixed pattern recognition task. d) Schematic diagram of training set and test set for single-color or mixed-color digits. e) Dependence of recognition rate from the NN and ONN on training epochs. f) Comparison of weight image after the 12th and 600th training epoch. g) Comparison of the activation of NN and ONN in cases of single-color number "1" or mixed-color number "4" after the 600th training epoch. Reproduced with permission.^[41] Copyright 2018, Springer Nature.

and pattern recognition. Despite optoelectronic synapses have experienced rapid development, many challenges are remaining, regarding to emulate the complex synaptic functions.

The generalized performance criteria have not been defined. Each of these devices has its own features and advantages, and the performance and energy consumption could be influenced by many factors, including the device structure, device dimensions, type of materials, and wavelength of light stimuli. Currently, most of the reported works are focused on the emulation of synaptic functions; however, these optoelectronic synaptic devices

are hard to be compared. Thus, the criteria should be established for evaluating the device performance, assisting to explore superior materials or structures for neuromorphic computing.

Inhibitory of PSC with optical signals is still a big challenge. The optoelectronic synapses rely on the photogenerated carriers to tune the synaptic weight, and it is difficult to achieve short-term/long-term depression or reset process by optical stimuli. Presently, the PSC depression is realized through the voltage pulse in the three-terminal optoelectronic synapses, which will make ANNs sophisticated and cause additional energy

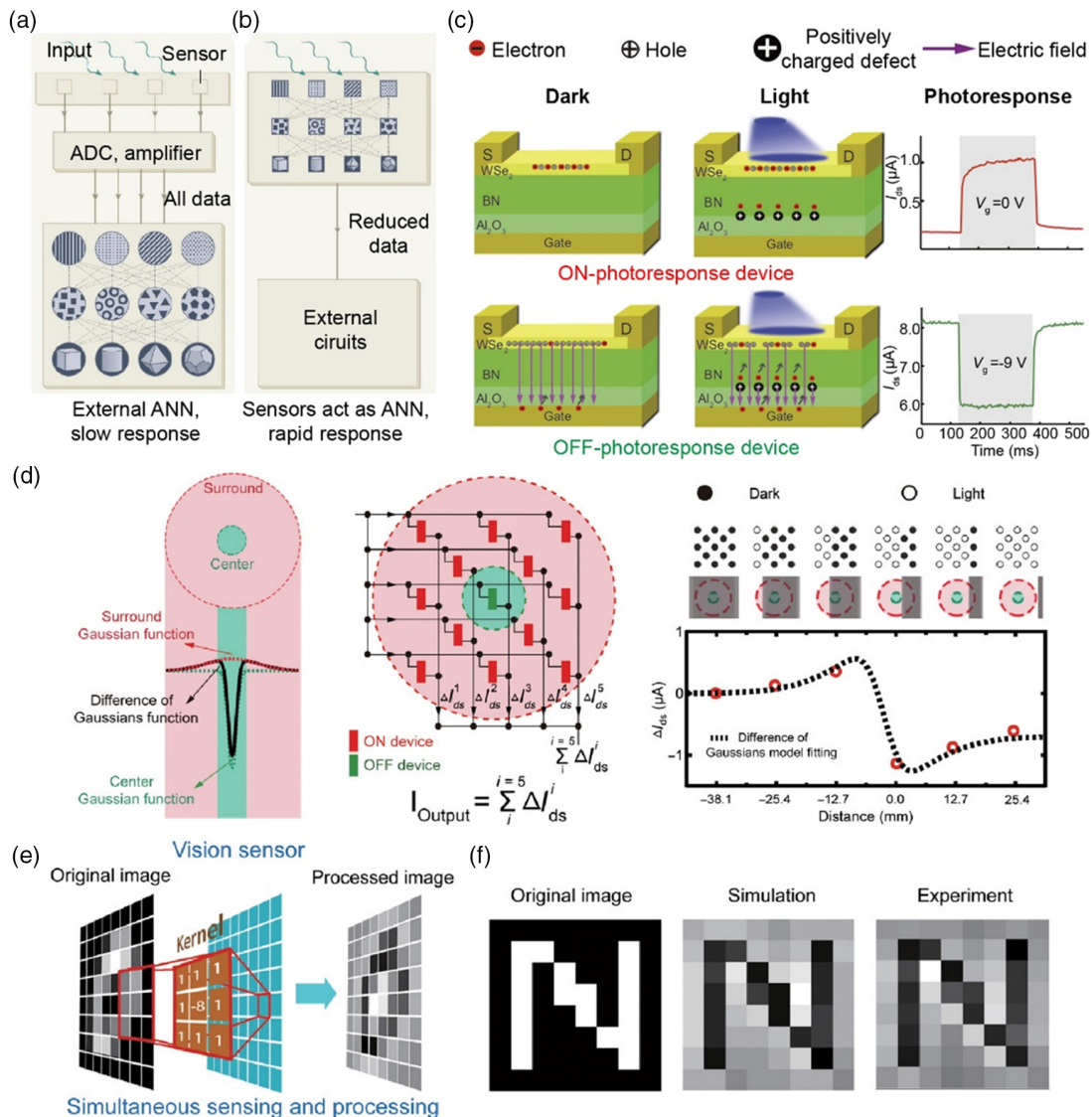


Figure 10. a) Schematic illustration of the data processing steps of a conventional AI vision sensor, in which the signals are collected by the photosensor, converted, and fed as inputs to the external ANN. The response is slow and energy-hungry. b) A novel AI vision sensor proposed by Mennel et al., showing the ability to collect signals as well as to recognize simple feature working as an ANN. The response is rapid due to avoiding the transition of redundant data between sensors and external circuits. a,b) Reproduced with permission.^[75] Copyright 2020, Springer Nature. c) Operation mechanism of the ON-/OFF-photoresponse device and corresponding photoresponse at the gate voltages of zero and -9 V, respectively. d) Emulation of the biological RF. Left panel: DGM of the RF for the characterization of the responsivity distribution. Middle panel: the configuration of vision sensor array with the OFF-photoresponse device in the center, surrounded by ON-photoresponse devices. Right panel: the artificial RF for edge of objects detecting. e) The vision sensor array for simultaneous sensing and processing. f) Edge enhancement of the "N" letter through the vision sensor. Left panel is the original image of the "N" letter. Middle and right panels are the simulation and experiment results, respectively. c–f) Reproduced with permission.^[76] Copyright 2020, American Association for the Advancement of Science.

consumption. Development of new functional materials or novel device architecture to realize the inhibitory optoelectronic synapses is urgently necessary.

The optoelectronic synapses usually work in the current range from tens of nanoamps to several microamps, which may lead to larger energy consumption per synaptic event than the biological level (1–100 fJ). Low-dimensional materials with high photosensitivity and small current amplitude could be exploited. Interface engineering and band engineering are also crucial for the

heterostructure-based optoelectronic synapses to decrease charge transfer loss. In addition, downscaling the device dimensions to the nanoscale can not only reduce energy consumption but also facilitate large-scale array integration for brain-like computing.

Although the optoelectronic synapses are currently in its initial stage to emulate the synaptic behavior, we expect that the breakthrough in the artificial visual-perception system and neuromorphic computing will be enabled through the interaction of neural science, materials science, and computer science in the future.

Acknowledgements

X.H. and Z.X. contributed equally to this work. The authors thank the support of national key R&D project from Minister of Science and Technology, China (2016YFA0202703), National Natural Science Foundation of China (No. 61675027, 51622205, 51432005, 61805015, and 61804011), Beijing City Committee of science and technology (Z171100002017019 and Z181100004418004), Beijing Natural Science Foundation (4181004, 4182080, 4184110, 2184131, and Z180011), and Shenzhen Science and Technology Program (Grant No. KQTD20170810105439418).

Conflict of Interest

The authors declare no conflict of interest.

Keywords

artificial visual-perception systems, neuromorphic computing, optoelectronic synapses, synaptic behaviors

Received: July 3, 2020

Revised: September 1, 2020

Published online:

- [1] a) D. Kuzum, S. Yu, H. P. Wong, *Nanotechnology* **2013**, *24*, 382001; b) M. D. Ventra, Y. V. Pershin, *Nat. Phys.* **2013**, *9*, 200.
- [2] a) G. Indiveri, S. C. Liu, *Proc. IEEE* **2015**, *103*, 1379; b) T. Hasegawa, T. Ohno, K. Terabe, T. Tsuruoka, T. Nakayama, J. K. Gimzewski, M. Aono, *Adv. Mater.* **2010**, *22*, 1831.
- [3] a) I. A. Basheer, M. Hajmeer, *J. Microbiol. Methods* **2000**, *43*, 3; b) D. Silver, A. Huang, C. J. Maddison, A. Guez, L. Sifre, G. V. Den Driessche, J. Schrittwieser, I. Antonoglou, V. Panneershelvam, M. Lanctot, *Nature* **2016**, *529*, 484.
- [4] a) P. A. Merolla, J. V. Arthur, R. Alvarezicaza, A. S. Cassidy, J. Sawada, F. Akopyan, B. L. Jackson, N. Imam, C. Guo, Y. Nakamura, *Science* **2014**, *345*, 668; b) X. Liao, L. Xiao, C. Yang, Y. Lu, *Front. Comput. Sci.* **2014**, *8*, 345; c) H. Markram, *Nat. Rev. Neurosci.* **2006**, *7*, 153.
- [5] C. Poon, K. Zhou, *Front. Neurosci.* **2011**, *5*, 108.
- [6] a) V. M. Ho, J. Lee, K. C. Martin, *Science* **2011**, *334*, 623; b) D. A. Drachman, *Neurology* **2005**, *64*, 2004.
- [7] a) A. E. Pereda, *Nat. Rev. Neurosci.* **2014**, *15*, 250; b) L. F. Abbott, W. G. Regehr, *Nature* **2004**, *431*, 796.
- [8] D. Choquet, A. Triller, *Neuron* **2013**, *80*, 691.
- [9] E. S. Fortune, G. J. Rose, *Trends Neurosci.* **2001**, *24*, 381.
- [10] a) S. F. Cooke, T. V. P. Bliss, *Brain* **2006**, *129*, 1659; b) D. M. Kullmann, K. Lamsa, *Nat. Rev. Neurosci.* **2007**, *8*, 687.
- [11] a) M. A. Lynch, *Physiol. Rev.* **2004**, *84*, 87; b) G. L. Collingridge, S. Peineau, J. G. Howland, Y. T. Wang, *Nat. Rev. Neurosci.* **2010**, *11*, 459.
- [12] a) N. Caporale, Y. Dan, *Annu. Rev. Neurosci.* **2008**, *31*, 25; b) G. Rachmuth, H. Z. Shouval, M. F. Bear, C. Poon, *Proc. Natl. Acad. Sci. U. S. A.* **2011**, *108*, 19453.
- [13] a) H. Han, H. Yu, H. Wei, J. Gong, W. Xu, *Small* **2019**, *15*, 1900695; b) S. Dai, Y. Zhao, Y. Wang, J. Zhang, L. Fang, S. Jin, Y. Shao, J. Huang, *Adv. Funct. Mater.* **2019**, *29*, 1903700; c) H. Y. Yu, H. H. Wei, J. D. Gong, H. Han, M. X. Ma, Y. F. Wang, W. T. Xu, *Small* **2020**, 2000041, <https://doi.org/10.1002/smll.202000041>.
- [14] a) M. Wuttig, N. Yamada, *Nat. Mater.* **2007**, *6*, 824; b) T. Lee, D. Loke, K. Huang, W. Wang, S. R. Elliott, *Adv. Mater.* **2014**, *26*, 7493.
- [15] a) S. H. Jo, T. Chang, I. Ebong, B. Bhadviya, P. Mazumder, W. Lu, *Nano Lett.* **2010**, *10*, 1297; b) Z. Wang, S. Joshi, S. Savelev, H. Jiang, R. Midya, P. Lin, M. Hu, N. Ge, J. P. Strachan, Z. Li, *Nat. Mater.* **2017**, *16*, 101; c) W. H. Qian, X. F. Cheng, J. Zhou, J. H. He, H. Li, Q. F. Xu, N. J. Li, D. Y. Chen, Z. G. Yao, J. M. Lu, *InfoMat* **2020**, *2*, 743.
- [16] a) W. Xu, H. Cho, Y. Kim, Y. Kim, C. Wolf, C. Park, T. Lee, *Adv. Mater.* **2016**, *28*, 5916; b) C. Ma, Z. Luo, W. Huang, L. Zhao, Q. Chen, Y. Lin, X. Liu, Z. Chen, C. Liu, H. Sun, *Nat. Commun.* **2020**, *11*, 1.
- [17] a) S. Yu, B. Gao, Z. Fang, H. Yu, J. Kang, H. S. P. Wong, *Adv. Mater.* **2013**, *25*, 1774; b) H. Tian, L. Zhao, X. Wang, Y. Yeh, N. Yao, B. P. Rand, T. Ren, *Acs Nano* **2017**, *11*, 12247.
- [18] a) S. Jiang, S. Nie, Y. He, R. Liu, C. Chen, Q. Wan, *Mater. Today Nano* **2019**, *8*, 100059; b) M. A. Zidan, J. P. Strachan, W. D. Lu, *Nat. Electron.* **2018**, *1*, 22.
- [19] G. Wang, R. Wang, W. Kong, J. Zhang, *Cogn. Neurodyn.* **2018**, *12*, 615.
- [20] a) R. Sabesan, B. Schmidt, W. S. Tuten, A. Roorda, *Sci. Adv.* **2016**, *2*, e1600797; b) H. L. Park, H. Kim, D. Lim, H. Zhou, Y. H. Kim, Y. Lee, S. Park, T. W. Lee, *Adv. Mater.* **2020**, *32*, 1906899.
- [21] H. Park, Y. Lee, N. Kim, D. Seo, G. Go, T. Lee, *Adv. Mater.* **2019**, *32*, 1903558.
- [22] X. Zhuge, J. Wang, F. Zhuge, *Phys. Status Solidi RRL* **2019**, *13*, 1900082.
- [23] a) Y. Zang, H. Shen, D. Huang, C. Di, D. Zhu, *Adv. Mater.* **2017**, *29*, 1606088; b) M. Lee, W. Lee, S. Choi, J. Jo, J. Kim, S. K. Park, Y. Kim, *Adv. Mater.* **2017**, *29*, 1700951.
- [24] a) M. Kumar, T. Som, J. Kim, *Adv. Mater.* **2019**, *31*, 1903095; b) W. Deng, X. Zhang, R. Jia, L. Huang, X. Zhang, J. Jie, *NPG Asia Mater.* **2019**, *11*, 77.
- [25] X. Zhu, W. Lu, *ACS Nano* **2018**, *12*, 1242.
- [26] a) H. Tan, G. Liu, X. Zhu, H. Yang, B. Chen, X. Chen, J. Shang, W. Lu, Y. Wu, R. Li, *Adv. Mater.* **2015**, *27*, 2797; b) H. Tan, G. Liu, H. Yang, X. Yi, L. Pan, J. Shang, S. Long, M. Liu, Y. Wu, R. Li, *ACS Nano* **2017**, *11*, 11298.
- [27] F. C. Zhou, Z. Zhou, J. W. Chen, T. H. Choy, J. L. Wang, N. Zhang, Z. Y. Lin, S. M. Yu, J. F. Kang, H. S. P. Wong, Y. Chai, *Nat. Nanotechnol.* **2019**, *14*, 776.
- [28] a) S. C. Qin, F. Q. Wang, Y. J. Liu, Q. Wan, X. R. Wang, Y. B. Xu, Y. Shi, X. M. Wang, R. Zhang, *2D Mater.* **2017**, *4*, 035022; b) R. A. John, F. Liu, N. A. Chien, M. R. Kulkarni, C. Zhu, Q. Fu, A. Basu, Z. Liu, N. Mathews, *Adv. Mater.* **2018**, *30*, 1800220; c) Z. Luo, X. Xia, M. Yang, N. R. Wilson, A. Gruverman, M. Alexe, *ACS Nano* **2020**, *14*, 746.
- [29] a) Y. Lee, J. Y. Oh, W. Xu, O. Kim, T. R. Kim, J. Kang, Y. Kim, D. H. Son, J. B. H. Tok, M. J. Park, *Sci. Adv.* **2018**, *4*, eaat7387; b) T. Leydecker, M. Herder, E. Pavlica, G. Bratina, S. Hecht, E. Orgiu, P. Samori, *Nat. Nanotechnol.* **2016**, *11*, 769.
- [30] L. Zhao, Z. Fan, S. Cheng, L. Hong, Y. Li, G. Tian, D. Chen, Z. Hou, M. Qin, M. Zeng, *Adv. Electron. Mater.* **2020**, *6*, 1900858.
- [31] S. Gao, G. Liu, H. Yang, C. Hu, Q. Chen, G. Gong, W. Xue, X. Yi, J. Shang, R. Li, *Acs Nano* **2019**, *13*, 2634.
- [32] H. Tan, Z. Y. Ni, W. B. Peng, S. C. Du, X. K. Liu, S. Y. Zhao, W. Li, Z. Ye, M. S. Xu, Y. Xu, X. D. Pi, D. R. Yang, *Nano Energy* **2018**, *52*, 422.
- [33] S. Y. Wang, C. S. Chen, Z. H. Yu, Y. L. He, X. Y. Chen, Q. Wan, Y. Shi, D. W. Zhang, H. Zhou, X. R. Wang, P. Zhou, *Adv. Mater.* **2019**, *31*, 1806227.
- [34] F. Sun, Q. Lu, L. Liu, L. Li, Y. Wang, M. Hao, Z. Cao, Z. Wang, S. Wang, T. Li, *Adv. Mater. Technol.* **2020**, *5*, 1900888.
- [35] Y. Wang, Z. Y. Lv, J. R. Chen, Z. P. Wang, Y. Zhou, L. Zhou, X. L. Chen, S. T. Han, *Adv. Mater.* **2018**, *30*, 1800327.
- [36] C. Qian, S. Oh, Y. Choi, J. H. Kim, J. Sun, H. Huang, J. L. Yang, Y. L. Gao, J. H. Park, J. H. Cho, *Nano Energy* **2019**, *66*, 104095.
- [37] Q. Wu, J. Wang, J. C. Cao, C. Lu, G. Yang, X. Shi, X. Chuai, Y. Gong, Y. Su, Y. Zhao, *Adv. Electron. Mater.* **2018**, *4*, 1800556.

- [38] K. Wang, S. Dai, Y. Zhao, Y. Wang, C. Liu, J. Huang, *Small* **2019**, *15*, 1900010.
- [39] H. Wang, Q. Zhao, Z. Ni, Q. Li, H. Liu, Y. Yang, L. Wang, Y. Ran, Y. Guo, W. Hu, *Adv. Mater.* **2018**, *30*, 1803961.
- [40] S. Chen, Z. Lou, D. Chen, G. Shen, *Adv. Mater.* **2018**, *30*, 1705400.
- [41] S. Seo, S. Jo, S. Kim, J. Shim, S. Oh, J. Kim, K. Heo, J. Choi, C. H. Choi, S. Oh, *Nat. Commun.* **2018**, *9*, 5106.
- [42] S. M. Kwon, S. W. Cho, M. Kim, J. S. Heo, Y. Kim, S. K. Park, *Adv. Mater.* **2019**, *31*, 1906433.
- [43] a) X. Han, W. Du, R. Yu, C. Pan, Z. L. Wang, *Adv. Mater.* **2015**, *27*, 7963; b) W. Wu, X. Wang, X. Han, Z. Yang, G. Gao, Y. Zhang, J. Hu, Y. Tan, A. Pan, C. Pan, *Adv. Mater.* **2019**, *31*, 1805913; c) L. L. Gu, S. Poddar, Y. J. Lin, Z. H. Long, D. Q. Zhang, Q. P. Zhang, L. Shu, X. Qiu, M. Kam, A. Javey, Z. Y. Fan, *Nature* **2020**, *581*, 278.
- [44] a) D. Bozyigit, W. M. M. Lin, N. Yazdani, O. Yarema, V. Wood, *Nat. Commun.* **2015**, *6*, 6180; b) Y. Mei, P. J. Diemer, M. R. Niazi, R. K. Hallani, K. Jarolimek, C. S. Day, C. Risko, J. E. Anthony, A. Amassian, O. D. Jurchescu, *Proc. Natl. Acad. Sci. U. S. A.* **2017**, *114*, 201705164.
- [45] H. K. Li, T. Chen, P. Liu, S. Hu, Y. Liu, Q. Zhang, P. S. Lee, *J. Appl. Phys.* **2016**, *119*, 244505.
- [46] A. J. Arnold, A. Razavieh, J. R. Nasr, D. S. Schulman, C. M. Eichfeld, S. Das, *ACS Nano* **2017**, *11*, 3110.
- [47] a) R. N. Pereira, J. Coutinho, S. Niesar, T. A. Oliveira, W. Aigner, H. Wiggers, M. J. Rayson, P. R. Briddon, M. S. Brandt, M. Stutzmann, *Nano Lett.* **2014**, *14*, 3817; b) P. Lu, W. W. Mu, J. Xu, X. W. Zhang, W. P. Zhang, W. Li, L. Xu, K. J. Chen, *Sci. Rep.* **2016**, *6*, 22888.
- [48] Z. Y. Ni, X. D. Pi, S. Cottenier, D. R. Yang, *Phys. Rev. B* **2017**, *95*, 075307.
- [49] L. Q. Zhu, C. J. Wan, L. Q. Guo, Y. Shi, Q. Wan, *Nat. Commun.* **2014**, *5*, 3158.
- [50] a) Z. Ni, L. Ma, S. Du, Y. Xu, M. Yuan, H. Fang, Z. Wang, M. Xu, D. Li, J. Yang, *ACS Nano* **2017**, *11*, 9854; b) D. Tan, K. N. Sharafudeen, Y. Yue, J. Qiu, *Prog. Mater. Sci.* **2016**, *76*, 154.
- [51] J. Kakalios, R. A. Street, W. B. Jackson, *Phys. Rev. Lett.* **1987**, *59*, 1037.
- [52] a) C. Groves, *Energy Environ. Sci.* **2013**, *6*, 1546; b) Y.-Y. Chen, C.-H. Wang, G.-S. Chen, Y.-C. Li, C.-P. Liu, *Nano Energy* **2015**, *11*, 533; c) R. Bao, C. Wang, L. Dong, R. Yu, K. Zhao, Z. L. Wang, C. Pan, *Adv. Funct. Mater.* **2015**, *25*, 2884; d) R. Bao, C. Wang, Z. Peng, C. Ma, L. Dong, C. Pan, *ACS Photonics* **2017**, *4*, 1344; e) R. Bao, C. Wang, L. Dong, C. Shen, K. Zhao, C. Pan, *Nanoscale* **2016**, *8*, 8078; f) C. Wang, R. Bao, K. Zhao, T. Zhang, L. Dong, C. Pan, *Nano Energy* **2015**, *14*, 364; g) J. R. Sun, Q. Hua, R. Zhou, D. Li, W. Guo, X. Li, G. Hu, C. Shan, Q. Meng, L. Dong, *ACS Nano* **2019**, *13*, 4507.
- [53] a) L. Qin, L. Wu, B. Kattel, C. Li, Y. Zhang, Y. Hou, J. Wu, W. Chan, *Adv. Funct. Mater.* **2017**, *27*, 1704173; b) C. Xie, F. Yan, *J. Mater. Chem. C* **2018**, *6*, 1338.
- [54] a) W. Huh, S. Jang, J. Y. Lee, D. Lee, J. M. Lee, H. Park, J. C. Kim, H. Y. Jeong, G. Wang, C. Lee, *Adv. Mater.* **2018**, *30*, 1801447; b) S. Shen, X. Wang, Y. Tian, M. Li, Y. Yang, T. Ren, *Nanoscale* **2019**, *11*, 11114.
- [55] a) J. Shi, S. D. Ha, Y. Zhou, F. Schoofs, S. Ramanathan, *Nat. Commun.* **2013**, *4*, 2676; b) C. J. Wan, L. Q. Zhu, J. M. Zhou, Y. Shi, Q. Wan, *Nanoscale* **2013**, *5*, 10194.
- [56] E. W. Lim, R. Ismail, *Electronics* **2015**, *4*, 586.
- [57] M. Lubben, P. Karakolis, V. Ioannousougliridis, P. Normand, P. Dimitrakis, I. Valov, *Adv. Mater.* **2015**, *27*, 6202.
- [58] L. Xiao, L. Zhuang, Y. Liu, J. Lu, H. D. Abruna, *J. Am. Chem. Soc.* **2009**, *131*, 602.
- [59] a) T. Tsuruoka, K. Terabe, T. Hasegawa, I. Valov, R. Waser, M. Aono, *Adv. Funct. Mater.* **2012**, *22*, 70; b) S. Wang, W. Fan, Z. Liu, A. Yu, X. Jiang, *J. Mater. Chem. C* **2018**, *6*, 191.
- [60] a) P. Feng, I. Monch, S. Harazim, G. Huang, Y. Mei, O. G. Schmidt, *Nano Lett.* **2009**, *9*, 3453; b) Y. Su, S. M. Peng, L. Ji, C. Z. Wu, W. B. Cheng, C. Liu, *Langmuir* **2010**, *26*, 603.
- [61] a) S. Lany, A. Zunger, *Phys. Rev. B* **2005**, *72*, 035215; b) F. Oba, A. Togo, I. Tanaka, J. Paier, G. Kresse, *Phys. Rev. B* **2008**, *77*, 245202.
- [62] S. Jeon, S. Ahn, I. Song, C. J. Kim, U. Chung, E. Lee, I. K. Yoo, A. Nathan, S. Lee, K. Ghaffarzadeh, *Nat. Mater.* **2012**, *14*, 452.
- [63] a) P. I. Reyes, C. J. Ku, Z. Duan, Y. Xu, E. Garfunkel, Y. Lu, *Appl. Phys. Lett.* **2012**, *101*, 031118; b) J. S. Park, T. S. Kim, K. S. Son, K. Lee, W. J. Maeng, H. Kim, E. S. Kim, K. Park, J. Seon, W. Choi, *Appl. Phys. Lett.* **2010**, *96*, 262109; c) M. Lee, M. Kim, J. Jo, S. K. Park, Y. Kim, *Appl. Phys. Lett.* **2018**, *112*, 052103.
- [64] D. H. Chowdhury, P. Migliorato, J. Jang, *Appl. Phys. Lett.* **2010**, *97*, 173506.
- [65] K. Ghaffarzadeh, A. Nathan, J. Robertson, S. Kim, S. Jeon, C. Kim, U. Chung, J. Lee, *Appl. Phys. Lett.* **2010**, *97*, 113504.
- [66] S. Ahn, I. Song, S. Jeon, Y. W. Jeon, Y. K. Kim, C. Kim, B. Ryu, J. Lee, A. Nathan, S. Lee, *Adv. Mater.* **2012**, *24*, 2631.
- [67] a) T. Iwasaki, N. Itagaki, T. Den, H. Kumomi, K. Nomura, T. Kamiya, H. Hosono, *Appl. Phys. Lett.* **2007**, *90*, 242114; b) S. Lee, A. Nathan, *Science* **2016**, *354*, 302.
- [68] a) X. Zhao, H. Xu, Z. Wang, Y. Lin, Y. Liu, *InfoMat* **2019**, *1*, 183; b) Z. Zhang, Z. Wang, T. Shi, C. Bi, F. Rao, Y. Cai, Q. Liu, H. Wu, P. Zhou, *InfoMat* **2020**, *2*, 261; c) F. M. Bayat, M. Prezioso, B. Chakrabarti, H. Nili, I. Kataeva, D. B. Strukov, *Nat. Commun.* **2018**, *9*, 2331.
- [69] a) Y. H. Liu, L. Q. Zhu, P. Feng, Y. Shi, Q. Wan, *Adv. Mater.* **2015**, *27*, 5599; b) Y. Kaneko, Y. Nishitani, M. Ueda, *IEEE Trans. Electron Devices* **2014**, *61*, 2827.
- [70] a) C. Pan, W. Guo, L. Dong, G. Zhu, Z. L. Wang, *Adv. Mater.* **2012**, *24*, 3356; b) H. L. Zhang, D. F. Peng, W. Wang, L. Dong, C. F. Pan, *J. Phys. Chem. C* **2015**, *119*, 28136.
- [71] a) H. Liu, Q. Li, Y. Bu, N. Zhang, C. Wang, C. Pan, L. Mi, Z. Guo, C. Liu, C. Shen, *Nano Energy* **2019**, *66*, 104143; b) K. Zhou, Y. Zhao, X. Sun, Z. Yuan, G. Zheng, K. Dai, L. Mi, C. Pan, C. Liu, C. Shen, *Nano Energy* **2020**, *70*, 104546; c) C. Wang, J. Zhao, C. Ma, J. R. Sun, L. Tian, X. Li, F. Li, X. Han, C. Liu, C. Shen, *Nano Energy* **2017**, *34*, 578.
- [72] J. Kim, A. S. Campbell, B. E. De Avila, J. Wang, *Nat. Biotechnol.* **2019**, *37*, 389.
- [73] a) C. Wang, C. Pan, Z. L. Wang, *ACS Nano* **2019**, *13*, 12287; b) X. Wang, H. Zhang, R. Yu, L. Dong, D. Peng, A. Zhang, Y. Zhang, H. Liu, C. Pan, Z. L. Wang, *Adv. Mater.* **2015**, *27*, 2324; c) R. Yu, L. Dong, C. Pan, S. Niu, H. F. Liu, W. Liu, S. J. Chua, D. Chi, Z. L. Wang, *Adv. Mater.* **2012**, *24*, 3532; d) Y. Peng, J. Lu, D. Peng, W. Ma, F. Li, Q. Chen, X. Wang, J. R. Sun, H. Liu, C. Pan, *Adv. Funct. Mater.* **2019**, *29*, 1905051; e) L. Dong, S. Niu, C. Pan, R. Yu, Y. Zhang, Z. L. Wang, *Adv. Mater.* **2012**, *24*, 5470; f) M. Que, W. Guo, X. Zhang, X. Li, Q. Hua, L. Dong, C. Pan, *J. Mater. Chem. A* **2014**, *2*, 13661.
- [74] a) M. Prezioso, F. Merrikhbayat, B. D. Hoskins, G. C. Adam, K. K. Likharev, D. B. Strukov, *Nature* **2015**, *521*, 61; b) S. Kim, J. Yoon, H. D. Kim, S. Choi, *ACS Appl. Mater. Interfaces* **2015**, *7*, 25479; c) S. Choi, S. H. Tan, Z. Li, Y. Kim, C. Choi, P. Chen, H. Yeon, S. Yu, J. Kim, *Nat. Mater.* **2018**, *17*, 335.
- [75] C. Yang, *Nature* **2020**, *579*, 32.
- [76] C. Y. Wang, S. J. Liang, S. Wang, P. F. Wang, Z. Li, Z. R. Wang, A. Y. Gao, C. Pan, C. Liu, J. Liu, H. F. Yang, X. W. Liu, W. H. Song, C. Wang, X. M. Wang, K. J. Chen, Z. L. Wang, K. Watanabe, T. Taniguchi, J. J. Yang, F. Miao, B. Cheng, *Sci. Adv.* **2020**, *6*, eaba6173.
- [77] L. Mennel, J. Symonowicz, S. Wachter, D. K. Polyushkin, A. J. Molina-Mendoza, T. Mueller, *Nature* **2020**, *579*, 62.



Xun Han received his B.S. degree (2012) from Shandong University and his Ph.D. degree (2017) from the Beijing Institute of Nanoenergy and Nanosystems, Chinese Academy of Sciences, China. He carried out postdoctoral research work at Northeastern University (U.S.). He joined Shenzhen University as a Research Associate Professor in 2019. His research interests mainly focus on the fields of piezo-phototronics effect for advanced optoelectronic devices.



Zhangsheng Xu received her B.S. degree from the China University of Mining and Technology (2018). He is an M.S. candidate in the Beijing Institute of Nanoenergy and Nanosystems, Chinese Academy of Sciences. His major research focus is on perovskite materials and their applications as image sensors and artificial visual system.



Peiguang Yan received his Ph.D. degree in the College of Physics Science from the Nankai University (China) in 2005. He joined the Shenzhen University (China) in 2005 as a Lecturer, and became an Associate Professor (2007–2012) and promoted to Professor from 2013. His current research interests include fiber optics, ultrafast fiber lasers, fiber sensors, and silicon photonics.



Caofeng Pan received his B.Sc. degree (2005) and Ph.D. (2010) degree in materials science and engineering from Tsinghua University, China. Then, he joined the group of Prof. Zhong Lin Wang at the Georgia Institute of Technology as a Postdoctoral Fellow. He has been a Professor and a Group Leader at the Beijing Institute of Nanoenergy and Nanosystems, Chinese Academy of Sciences, since 2013. His research interests mainly focus on the fields of piezotronics/piezo-phototronics for fabricating new electronic and optoelectronic devices, nanopower sources, hybrid nanogenerators, and self-powered nanosystems.